

Variability of intraseasonal Kelvin waves in the equatorial Pacific Ocean

Toshiaki Shinoda

NOAA-CIRES Earth System Research Laboratory

325 Broadway

Boulder, CO 80305

toshiaki.shinoda@noaa.gov

Fax: 303-497-6449

Tel: 303-497-4295

Paul E. Roundy

Department of Earth and Atmospheric Sciences

University at Albany

State University of New York

George N. Kiladis

NOAA-CIRES Earth System Research Laboratory

J. Phys. Oceanogr. (in press)

February 11, 2008

Abstract

Previous observational work has demonstrated that the phase speed of oceanic equatorial Kelvin waves forced by the Madden-Julian oscillation (MJO) appears to vary substantially. Processes that are responsible for systematic changes in the phase speed of these waves are examined using an ocean general circulation model. The model was integrated for 26 years with daily wind stress derived from the NCEP-NCAR reanalysis. The model is able to reproduce observed systematic changes of Kelvin wave phase speed reasonably well, providing a tool for the analysis of their dynamics.

The relative importance of the upper ocean background state and atmospheric forcing for phase speed changes is determined based on a series of model experiments with various surface forcings. Systematic changes in phase speed are evident in all model experiments that have different slowly varying basic states, showing that variations of the upper ocean background state are not the primary cause of the changes. The model experiments that include and exclude intraseasonal components of wind stress in the eastern Pacific demonstrate that wind stress changes to the east of the dateline can significantly alter the speed of Kelvin waves initially generated over the western Pacific, which often results in a phase propagation faster than the free wave speed. These faster waves contribute to the systematic changes of phase speed evident in observations. Similar results are also obtained using a linear stratified model, eliminating nonlinearity as a possible cause of the phase speed changes.

1. Introduction

The Madden-Julian oscillation (MJO; Madden and Julian 1972, 1994) provides a significant source of fluxes of momentum and heat into the western Pacific Ocean (e.g., Zhang 1996, Shinoda et al. 1998). The zonal wind stress anomalies near the equator associated with the MJO often drive large upper ocean responses including strong anomalous currents and changes in thermocline depth (e.g., Ralph et al. 1997, Shinoda and Hendon 2001, Lengaigne et al. 2002, Waliser et al. 2003). These wind-induced signals propagate eastward along the equator as Kelvin waves, which cause prominent intraseasonal variability of the upper ocean and sea surface temperature (SST) in the central and eastern Pacific (e.g., Enfield 1987, Spillane et al. 1987, Kessler et al. 1995, Hendon et al. 1998, McPhaden 2002). Recent studies suggest that these intraseasonal Kelvin waves produced by the MJO play an important role in the onset and development of some El Niño events (e.g., McPhaden and Yu 1999, Kessler and Kleman 2000, Bergman et al. 2001).

In the past several years, intraseasonal Kelvin waves generated by the MJO have been extensively examined by various observational and modeling studies because of their potential importance for longer time-scale climate variability tied to ENSO (e.g., Kessler et al. 1995, Hendon et al. 1998, McPhaden 2002, Zhang and Gottschalck 2002, Cravatte et al. 2003, Roundy and Kiladis 2006). One of the unresolved issues regarding Kelvin waves associated with the MJO is that there is an apparent discrepancy of dominant periods in these processes. While the period of the MJO is about 40-50 days (e.g., Madden and Julian 1972, Salby and Hendon 1993), the spectral peak of oceanic Kelvin waves is centered at around 70 days (e.g., Enfield 1987; McPhaden and Taft 1988, Kessler et al. 1995). Recent studies provide some reconciliation of this discrepancy based on the analyses of TOGA TAO mooring array data (Kessler et al.

1995, Hendon et al. 1998, Roundy and Kiladis 2006). Kessler et al. (1995) offered an explanation using a patch of oscillating zonal winds in the western Pacific. The Kelvin wave amplitude east of the patch is sensitive to the integrated forcing along the wave characteristics, and thus depends on the frequency of the forcing and the width of the patch. They showed that for a patch width typical of zonal wind anomalies associated with MJO, there is a rapid fall-off in Kelvin wave amplitude between roughly 100-day and 30-day periods, and argue that this accounts for the discrepancy of dominant periods between the MJO and oceanic Kelvin waves. Hendon et al. (1998) improved upon this simple patch model by including the eastward propagation of wind anomalies associated with the MJO. They showed that the maximum of Kelvin wave amplitude occurs at periods around 70 days for realistic propagating wind anomalies.

Roundy and Kiladis (2006; referred to as RK06 hereafter) proposed that an alternative process might be responsible for the discrepancy, which is of particular interest to the present study. They analyzed 16 years of TOGA TAO data to describe the nature of intraseasonal Kelvin waves and their relationship to atmospheric forcing, and frequently observed a systematic decrease in Kelvin wave phase speed over time. Figure 1 shows unfiltered and 20-100 day filtered dynamic height anomalies from the TOGA TAO buoy measurements during spring and summer 2002 (RK06). During this period, a series of large scale convective and surface wind anomalies associated with the MJO passed over the tropical Indian and western Pacific Oceans. The wind anomalies generated a series of eastward-moving intraseasonal disturbances in the upper ocean shown in Fig. 1. RK06 also analyzed upper ocean velocity and temperature data during this period, showing that their dynamical structure is consistent with equatorial Kelvin waves propagating within and above the thermocline. A striking feature of Fig. 1 is the change of the wave phase speed with time. While the

phase speed of the downwelling Kelvin wave observed in late May to early June is ~ 3.8 m/s, the one generated in July moved at about ~ 2.7 m/s. These systematic changes of phase speed result in an increase in period of waves toward the east. The period of these waves in the western Pacific ($\sim 170^\circ\text{E}$ - 180°) is about 50-days which is close to the dominant period of the MJO, while that in the eastern Pacific is about 70 days, providing a mechanism that could translate the 40-50 day forcing over the western Pacific into lower frequency Kelvin waves in the east. RK06 also show that similar decreases of Kelvin wave of phase speed evident in Fig. 1 are often observed in other periods based on a composite analysis using 16 years of TAO data. This systematic behavior was also confirmed for an earlier record of island sea level data going back to 1974 (Roundy and Kiladis 2007; hereafter RK07).

While it is difficult to examine the mechanisms causing these phase speed changes based only on the analyses of observational data, several processes that could be important are discussed in RK06. For a “free” wave, that is, one initially forced by the MJO but then propagating through a steady stress field, basic state changes could potentially be important. These include a temporal or spatially varying thermocline depth or Equatorial Undercurrent (EUC). Alternatively, nonlinearity or a change to a dominance of a higher baroclinic mode could also be factors altering the wave as it evolves.

RK06 also found evidence for coupling between convection and SST that tended to systematically slow Kelvin wave phase speeds during the development of El Niño. Another possibility is that the waves are altered by wind stress along its path of propagation. Such “forced Kelvin waves” have been studied in the context of storm surges associated with Kelvin waves trapped along coastlines (see Gill 1982).

In this study, the processes responsible for some of the phase speed changes identified by RK06 are examined using ocean general circulation model (OGCM) and simple

model experiments. A series of OGCM experiments using different configurations of surface forcing is conducted to determine the relative importance of upper ocean basic state and atmospheric forcing for the phase speed changes. Similar experiments are repeated using a linear, continuously stratified model developed by McCreary (1981). These experiments demonstrate the importance of wind stress changes along the path of eastward-propagating oceanic disturbances such as those shown in Fig. 1. In this paper, as in RK06 and RK07, we retain the term “Kelvin wave” to describe even the fastest intraseasonal equatorial disturbances we observe, while acknowledging that the structure of these forced waves may deviate significantly from theoretical free Kelvin waves derived from the shallow water equations (Matsuno 1966; Moore and Philander 1977).

In the next section, OGCM control experiments and a comparison with the data are described. Section 3 describes the OGCM experiments designed to examine the extent to which the upper ocean basic state affects the Kelvin wave phase speed. In Section 4, the influence of atmospheric forcing on the phase speed changes is discussed based on additional model experiments. Also, results of the linear stratified model are used to confirm the results of OGCM experiments. Conclusions are provided in Section 5.

2. Ocean General Circulation Model and control experiments

2.1 Ocean General Circulation Model

The OGCM used in this study is the HYbrid Coordinate Ocean Model (HYCOM, Bleck 2002, Chassignet et al. 2003). The hybrid coordinate is isopycnal in the open, stratified ocean, but smoothly reverts to a terrain-following coordinate in shallow coastal regions, and to z-level coordinates in the mixed layer and/or unstratified seas. The K-Profile parameterization (KPP; Large et al. 1994) is used for vertical mixing in the model.

The model domain covers the tropical Indo-Pacific basin, between 30°N and 30°S. A stretched horizontal grid is used to allow for increased resolution near the equator with 16 vertical isopycnal (σ) layers. The meridional grid spacing smoothly increases from 0.25° at the equator to about 1° at 30°N and 30°S. The zonal grid resolution is uniform 1°. Open boundary conditions are employed along the northern and southern boundaries.

2.2 Surface forcing fields

The model is forced with daily surface fluxes estimated from the NCEP/NCAR reanalysis (Kalney et al. 1996) during 1979-2004 (referred to as the control experiment hereafter). Surface wind stress is estimated from daily winds at 10 m, specific humidity and air temperature at 2 m and SST from the NCEP/NCAR reanalysis utilizing the standard bulk formulae (Large and Pond 1981). Latent and sensible heat fluxes are calculated in a same manner except using the model SST at each time step. The net surface shortwave and longwave radiation and precipitation are derived from the NCEP/NCAR reanalysis. Previous studies evaluated NCEP winds on the intraseasonal time scale by comparison with in-situ and satellite-derived data (e.g., Shinoda et al. 1999; Jiang et al. 2005; Serra et al. 2007). Aspects relevant to the present

study are examined based on a comparison with in-situ data, and results are summarized in Appendix A. This comparison shows that intraseasonal wind variability in the western Pacific from the NCEP/NCAR reanalysis agree reasonably well with that from in-situ and scatterometer measurements. NCEP/NCAR reanalysis winds are available for a long time period with no spurious discontinuities due to changes in the assimilation scheme, and thus they are suitable for the present study that includes model integrations over 20 years.

It should be noted that shortwave and longwave radiation from the NCEP/NCAR reanalysis may have significant errors on intraseasonal time scales (Shinoda et al. 1999). Also, the diurnal cycle of shortwave radiation impacts intraseasonal SST in the warm pool (Shinoda and Hendon 1998, Shinoda 2005). However, this study investigates only the dynamical ocean response (Kelvin waves) to the atmospheric intraseasonal oscillation, and does not discuss SST variability associated with Kelvin waves. Hence the use of daily mean radiation from the NCEP/NCAR reanalysis is appropriate for this particular study.

2.3. Comparison of control experiment with observations

The model was first spun up using climatological forcing for 50 years from initial conditions based on climatological temperature and salinity (Levitus and Boyer 1994, Levitus et al. 1994). Then the model was integrated for two 26 year cycles (1979-2004), with the second cycle continuing from the end of the first cycle. The output with 3-day sampling for the 24-yr period (1981-2004) in the second cycle integration was analyzed.

Model simulations of tropical Oceans using HYCOM were previously evaluated by comparing with in-situ and satellite observations (e.g., Shaji et al. 2005, Han 2005, Han et al. 2006). These studies indicate that HYCOM is able to simulate tropical

upper ocean variability reasonably well, including that on the intraseasonal time scale. In this study, intraseasonal variability in the equatorial Pacific (2°N - 2°S), which is mostly caused by Kelvin waves, is compared with the TOGA TAO mooring data (McPhaden 1995) to examine the model's ability to simulate Kelvin waves generated by intraseasonal wind anomalies.

Overall activity of intraseasonal Kelvin waves in the model is first compared with that from the TAO mooring data for the period 1991-2004 when the spatial coverage of the TAO data is relatively good. The activity of Kelvin waves in each year is measured by the daily standard deviation of 20-100 day filtered (via a Lanczos digital filter) sea surface height (for the model) and dynamic height (for the TAO) anomalies from December through April when intraseasonal Kelvin waves are most active (e.g., Kessler et al. 1995). Interannual variations of overall activity (Fig. 2) are well simulated by the model ($rr = 0.91$) although the activity is somewhat weaker ($\sim 25\%$) than observations (see the caption of Fig. 2 for the magnitudes).

The intraseasonal SSH variation in the model is also compared with the observed dynamic height variation at each TAO mooring site on the equator. Figure 2b shows the correlation coefficients between the intraseasonally filtered (20-100 day) SSH from the model and the dynamic height from the TAO data at 8 mooring stations along the equator for the period 1992-2004. While correlations at all stations shown in the figure are statistically significant at the 99% confidence level, a large zonal variation in the correlation is evident. The model SSH is well correlated with the TAO data between 165°E and 155°W ($rr \sim 0.7$) where the largest amplitude Kelvin waves are often observed (e.g., Hendon et al. 1998). The correlations are much weaker east of 125°W , possibly because the amplitudes of wind-forced Kelvin waves are generally much weaker, and a significant fraction of intraseasonal variance in this region is also caused by internal variability such as instability waves and reflected Rossby waves.

Individual Kelvin waves during 1996-97 winter, when strong activity is observed, are also compared (Figure 3). Large downwelling Kelvin waves during early January and March generated by strong westerlies associated with the MJO are simulated reasonably well by the model. However, the Kelvin wave during January is somewhat weaker than observed. This discrepancy could be caused partly by a deficiency in NCEP winds in capturing the detailed spatial structure of the zonal wind anomalies along with the inability of model to represent physical processes such as upper ocean mixing. Nevertheless, the model reproduces intraseasonal variability near the equator observed by the TAO mooring reasonably well, and thus the model is suitable for the present study.

2.4. Kelvin waves during 2002

A case study by RK06 discussed Kelvin waves generated by the MJO forcing during boreal spring and summer 2002. As shown in Fig. 1, a systematic phase speed change of intraseasonal Kelvin waves is particularly prominent during this period. The model output is analyzed to examine whether the similar phase speed changes to those in the TAO data are evident.

Figure 4a shows intraseasonally filtered SSH anomalies from the control experiment. As in the analysis of TAO mooring data (Fig. 1), the phase speeds of successive Kelvin waves progressively decrease with time. The phase speeds are objectively measured by local maxima and minima of filtered SSH fields described in the Appendix B. The upwelling Kelvin wave during May is faster than ~ 5.0 m/s, whereas the wave during July-August is about 3.4 m/s. These changes of phase speed are consistent with the observations (Fig. 1) although overall phase speeds in the model are actually somewhat faster than the observed. The decrease of phase speed results in an increase of the period of Kelvin waves towards the east. The results indicate that the

model is able to simulate the observed change of Kelvin wave phase speed during this period at least in a qualitatively correct fashion.

Figure 4b shows the intraseasonally filtered surface zonal current anomalies near the equator during the same period, when similar changes of phase speed with time to those in SSH anomalies are evident. The relationship between SSH and zonal current anomalies is consistent with that of Kelvin waves. For example, large positive SSH anomalies centered around 150°W - 140°W during early June and late July are associated with strong anomalously eastward currents. However, further quantitative comparisons of this relationship is more difficult since zonal current anomalies on the equator include signals of both Kelvin and Rossby waves.

Figure 5 shows the vertical structure of total zonal velocity and 20-100 day filtered anomalies during mid-2002 at the equator, 140°W . Both total zonal currents and intraseasonal anomalies in the model compare favorably with observations at the same location (see Fig. 2 in RK06). A strong Equatorial Undercurrent (EUC) observed from mid-July to early August is well simulated by the model. Observed intraseasonal zonal current anomalies, which are strongest at the surface and in the main thermocline, are also well reproduced by the model. Anomalous eastward (westward) flow is associated with the crests (troughs) of SSH anomalies shown in Fig. 4, suggesting that these perturbations in the 20-100 day band simulated by the model are at least approximately consistent with Kelvin waves propagating in and above the thermocline. This is true even for the relatively fast upwelling wave in early May.

We will show in Section 4 that these eastward propagating perturbations are modified by wind stress as they propagate, and thus their detailed structure may deviate from that associated with free waves. We also show in Appendix C that in fact the Kelvin wave phase speed changes produced by the model experiments are rather sensitive to subtle differences in intraseasonal winds when different wind data

sets are used.

3. Effect of the upper ocean basic state

RK06 speculated on several processes that could affect Kelvin wave propagation. In particular, they discussed the possible effect of background currents and the depth of the thermocline. For example, the EUC could influence the Kelvin wave phase speed through advection since the strongest current is located in the thermocline where the vertical displacement associated with the waves tends to be greatest. Also, a deeper thermocline could cause faster eastward propagation (e.g., Long and Chang 1990, Benestad et al. 2002). In this section, the effect of a slowly varying background state on Kelvin wave phase speed is examined through a series of model experiments.

3.1 Experiment design

Three sets of model experiments with different surface wind stress fields were conducted to elucidate whether the upper ocean basic state significantly influences the Kelvin wave phase speed. In the first experiment (referred to as EX-1), surface stresses are calculated as the summation of the annual cycle, 20-100 day filtered anomalies, and 100-day low-pass filtered anomalies. The stress anomalies are first computed by subtracting the annual cycle stress (first three harmonics of the seasonal cycle), then band-pass (20-100 day) and low-pass (100-day) filters are applied to the time series of anomalies. In this experiment, the upper ocean basic state varies annually and interannually primarily in response to the annual cycle stress and 100-day low-pass filtered anomalies, and intraseasonal Kelvin waves are generated by the 20-100 day filtered anomalies. The second experiment (EX-2) uses the wind stresses that are the summation of annual cycle and 20-100 day filtered anomalies. The basic state changes annually in this experiment, but interannual variations such as ENSO warm and cold events are not generated. In the third experiment (EX-3), the stresses are calculated by adding 20-100 day filtered anomalies to annual mean values. The basic

state is nearly constant in time in this experiment and intraseasonal Kelvin waves are produced by 20-100 day filtered anomalies. Air temperature, specific humidity and precipitation in EX-1 and EX-2 are the climatological annual cycle and those in EX-3 are the annual mean in order to only examine the effect of wind stress. As a result of the identical intraseasonal stress anomalies, Kelvin waves with similar amplitude are generated in all three sets of experiments, but varying longer time scale forcing (> 100 days) will modify the characteristics of Kelvin waves through changes in the basic state.

3.2 Results

In order to describe slowly varying background states of the upper ocean in the model experiments, a 100-day low pass filter is first applied to SSH and velocity from the model output. Figure 6 shows the low-pass filtered SSH during spring and summer 2002 from EX-1, EX-2 and EX-3. Since this period includes the development stage of the 2002 El Nino event, significant differences in low pass filtered SSH between EX-1 and EX-2 are evident due to changes in interannual forcing. Also, slowly varying SSHs in EX-1 are consistent with the observation shown in Fig. 1. During the development of El Nino, SSH gradually increases in the central and eastern Pacific and decreases in the western Pacific. As a result, the SSH in EX-1 during August is higher than that in EX-2 in the central and eastern Pacific. Also, because of the inclusion of annual variability in the forcing, SSH in EX-2 is significantly different from that in EX-3. While SSH in EX-3 is almost constant in time, SSH decreases in the western Pacific in EX-2 during June-July. These differences in SSH result in a steeper east-west SSH slope in EX-3 during August. It should also be noted that the slowly varying SSH in the control experiment is similar to that in EX-1 (not shown).

Figure 7 shows the low-pass filtered zonal velocity at a depth of the 20°C isotherm

from these experiments. The 20°C isotherm is located in the middle of the thermocline where the EUC is found. The EUC variation in EX-1 is consistent with the TAO array measurement at 140°W (see Fig. 2 in RK06), in which a strong EUC (>100 cm/s) is observed in late July. This EUC variation is similar to that in the control experiment (not shown). There are significant differences in the EUC during this period between these experiments. While the EUC is nearly constant in time at each location in EX-3, it varies by about 30 cm/s at some locations in EX-1 and EX-2. For example, the zonal velocity is around 80 cm/s in the central Pacific near the dateline during mid-June in EX-1, and it is reduced to near 50 cm/s in late August.

Figure 8 shows the band-pass filtered SSH from these experiments during spring and summer 2002. While there are some minor differences between the runs, a similar decrease in Kelvin wave phase speed is evident in all experiments. Also, overall results of experiments EX-1, EX-2 and EX-3 are similar to those in the control run (Fig. 5). This indicates that variations of the upper ocean basic state are not the primary cause of the phase speed changes simulated by the model. Although significant annual and interannual variations of the EUC and SSH are evident during this period (Fig. 6, Fig 7), the magnitude of these anomalous currents and thermocline depth changes do not appear to be sufficiently large to cause the dominant changes of Kelvin wave propagation. For example, the magnitude of EUC variations is 20-35 cm/s during this period, which is much smaller than the phase speed changes in of observed and simulated Kelvin waves. Hence variations in the EUC could not have caused the observed phase speed differences of >2 m/s through advection. The results are also consistent with previous studies suggesting that the equatorial current system contributes little to Kelvin wave phase speeds (e.g., Philander 1979, Johnson and McPhaden 1993).

4. Effect of atmospheric forcing

Strong intraseasonal wind variability west of the dateline is primarily responsible for generating intraseasonal Kelvin waves. While intraseasonal wind variability is somewhat weaker east of the dateline, it is not insignificant. We now test whether the intraseasonal winds in the central and eastern Pacific could modify the phase speed of Kelvin waves through forcing by the wind stress.

4.1 Experiment design

In the previous section, it was demonstrated that the model forced with intraseasonal wind stress anomalies added to the annual mean values (EX-3) is able to simulate the observed phase speed changes of Kelvin waves. In order to examine the effect of intraseasonal winds in the eastern Pacific, the intraseasonal component (20-100 days) of wind stress east of 170°W is removed. In this experiment, the same wind stress in EX-3 is used west of 170°W , and the wind stress is linearly interpolated to annual mean values between 170°W and 160°W . The annual mean stress (without the intraseasonal component) is used east of 160°W . This experiment is referred to as EX-4 hereafter.

4.2 Results

a. Case study: spring/summer 2002

Figure 9 compares intraseasonally filtered (20-100 day) SSH anomalies near the equator during spring and summer 2002 in EX-3 with those in EX-4 along with the total zonal wind stress used in each experiment. While similar Kelvin waves are generated west of the dateline in both experiments, phase speed changes are not evident east of 160°W in EX-4. The phase speed of all Kelvin waves in EX-3 during this period are faster than those in EX-3 in the eastern Pacific. This indicates that relatively weak

intraseasonal wind anomalies east of the dateline influence the Kelvin wave phase speed, at least in the model. The phase speed of downwelling and upwelling Kelvin waves in the eastern Pacific in EX-4 is ~ 2.7 m/s, which is indistinguishable from the free wave speed of first baroclinic mode in this region.

Strong intraseasonal variations of zonal stress west of the dateline (Fig. 9) generate similar Kelvin waves in both experiments. A slight decrease of Kelvin wave speed with time is evident in both experiments in the generation region west of the dateline, since the same intraseasonal stress anomalies are used in this area. East of the dateline, there are significant intraseasonal stress anomalies that are excluded in the forcing in EX-4. Westerly anomalies during mid to late May are seen throughout the entire equatorial Pacific. Although intraseasonal winds east of the dateline are weaker than those in the generation region, the magnitude of these westerlies are comparable to the westerly wind event in the western Pacific that generated a downwelling Kelvin wave during this period. Hence it appears that these intraseasonal wind anomalies in the eastern Pacific can continuously distort the Kelvin waves as they propagate eastward.

In contrast to the westerly anomalies observed in May, the intraseasonal stress anomalies after mid-June in the eastern Pacific were weaker than those in the western Pacific. In that case, strong westerlies in the western Pacific generated a large amplitude downwelling Kelvin wave, and much weaker intraseasonal winds east of the dateline did not effectively distort this wave as it propagated eastward. As a result, the phase speed of Kelvin waves during May is faster than the strong downwelling Kelvin waves in July in EX-3. Therefore these experiments indicate that even relatively weak intraseasonal winds east of the dateline can modify Kelvin wave propagation, often resulting in a phase speed faster than the free wave speed.

b. Regression composite

In order to examine general characteristics of Kelvin wave propagation and their relation with atmospheric forcing, a regression model developed by RK06 is applied using the SSH anomalies from the OGCM experiments and the zonal wind stress used to force the model for the entire period of the experiments (1981-2004). As in RK06, the model is based on the Kelvin wave index time series (k) which are the intraseasonally filtered (20-100 days) SSH at the equator and the dateline. Filtered SSH and unfiltered wind stress are each treated as dependent variables (y) and are estimated using the following form:

$$y = a_0 + a_1k + a_2k^2 + a_3k^3 + a_4k^4 + \epsilon$$

where coefficients a_x are regression parameters, and ϵ represents the model residuals. It should be noted that RK06 use a more complex form of the regression model that includes the state of ENSO and ENSO trend indices. Since this study does not emphasize the relationship with ENSO, terms which include these indices as well as other higher order terms are removed from the original equation used in RK06. Further details of this method are discussed in RK06.

Figure 10 displays the regression composite from EX-1, EX-3 and EX-4. The phase speeds of Kelvin waves east of the dateline are measured as in Appendix B by identifying local maxima and minima at each 10° bin between 170°W and 110°W . Prior to the downwelling Kelvin wave evident at around lag zero, a faster propagating upwelling Kelvin wave is found in EX-1 and EX-3. The difference in phase speed between these upwelling and downwelling Kelvin waves is not evident in EX-4. In particular, the arrival of the crests and nodes of the waves in the eastern Pacific is substantially delayed in EX-4, providing statistical confirmation that the phase speed of Kelvin waves in the OGCM can be substantially modified by wind stress over the

eastern Pacific. These results are consistent with the 2002 case study discussed above, when significant easterlies in the eastern Pacific resulted in the decrease of Kelvin wave phase speed over time during this period (compare Figs. 1 and 9).

We also examined the relation between upwelling Kelvin waves generated by easterly anomalies and prior downwelling Kelvin waves, based on the same regression analysis. The relationship is nearly identical to Fig. 10 (with opposite signs) including the changes of Kelvin wave phase speed and the zonal variation of wind stress (not shown). This indicates that significant intraseasonal westerly anomalies in the eastern Pacific (such as occurred in late May 2002) that can generate fast downwelling Kelvin waves are often observed prior to easterly anomalies and upwelling Kelvin waves.

c. Wavenumber-frequency spectral analysis

In previous sections, it was demonstrated that waves propagating eastward faster than the free Kelvin wave speed can result from continuous wind stress east of the dateline. In this section, the influence of eastern Pacific wind forcing on intraseasonal SSH disturbances is verified by considering the dispersion relation of Kelvin waves based on the wavenumber-frequency spectral analysis. Wheeler and Kiladis (1999) demonstrated that wavenumber-frequency spectral analysis is useful for identifying signals of atmospheric equatorial waves, and for isolating their structure. The same technique used in Wheeler and Kiladis (1999) is applied to the model output to further examine the characteristics of oceanic Kelvin wave in each experiment.

Figure 11 shows contours of the base 10 logarithm of power in wavenumber-frequency space calculated using SSH anomalies in the equatorial area (2°N - 2°S) east of 170°W from the control experiment. A prominent Kelvin wave spectral signal is evident, with its peak corresponding to a phase speed of around 2.7 m/s, consistent with the first baroclinic mode. Higher baroclinic Kelvin modes (second through

4th) are also detected. In the negative (westward) wavenumber domain, a spectral peak near the dispersion curve of the equatorial Rossby wave is evident. Note that the background spectrum has not been removed in this analysis since the signals of equatorial waves are sufficiently strong to identify them in the raw spectrum.

Figure 12a and 12b display the spectra for the period range of 33-100 days for EX-3 and EX-4 respectively. While both spectra show the maxima at the nearly same location (\sim wavenumber 3, \sim frequency 0.016 cpd), the peaks around the Kelvin wave dispersion line are distinctly broader for EX-3. This difference is more prominent in the faster (left) side of the dispersion line, which includes phase speeds faster than 5 m/s. For example, the contour lines around the level 6.5-7.0 log scale at frequencies 0.014-0.026 cpd are nearly parallel to the Kelvin wave dispersion line for EX-4 in contrast to the contour lines of the same level for EX-3. These results again confirm that intraseasonal wind forcing east of the dateline can generate Kelvin waves faster than the free wave speed.

Another distinct difference in these figures is the signal of second baroclinic mode Kelvin wave. The maximum of the spectrum is evident around wavenumber 8, frequency \sim 0.017 cpd in Fig. 12b which corresponds to the second baroclinic mode Kelvin wave. On the other hand, first and second baroclinic modes are not clearly separated by the analysis for EX-3 (Fig. 12a). This suggests that second baroclinic mode Kelvin waves are also significantly distorted by wind forcing in the eastern Pacific. Characteristics and behavior of these higher baroclinic mode Kelvin waves identified by the spectral analysis are not discussed further in this paper, but will be pursued in future studies.

d. Linear stratified model experiments

RK06 discussed several potential mechanisms that could be responsible for systematic changes in the phase speed of observed Kelvin waves, one being the effect of nonlinear upper ocean processes such as those discussed in Fedorov and Melville (2000). While our OGCM experiments demonstrate the important role of atmospheric forcing, HYCOM includes nonlinear terms which might possibly influence the Kelvin wave phase speed. In this section, linear model experiments forced with an idealized wind field are used to confirm the importance of wind forcing for modifying the phase speed of Kelvin waves.

The model used in this study is the linear, continuously stratified model described by McCreary (1980, 1981) for the tropical Pacific basin (30°N-30°S). The equations of motion are linearized about a state of rest with a realistic background stratification. Solutions are represented as the normal mode expansions of the system. The characteristic speeds c_n for each baroclinic mode are estimated from buoyancy frequency N_b based on observations in the equatorial Pacific Ocean. The first two modes of c_n are $c_1=2.71$ m/s and $c_2=1.64$ m/s, which are close to those in observations (e.g., Cravatte et al. 2003) and in OGCM experiments (Fig. 12). Since the dominant signal on the equator in the OGCM experiments is found to be the first baroclinic mode Kelvin wave (Fig. 11, Fig. 12), only the first mode is considered in the linear model. To remove the signal of reflected Rossby waves, a damper at the eastern boundary is applied as described in McCreary et al. (1996) and Han et al. (1999).

The model was forced with sinusoidal zonal wind stress described as:

$$\begin{aligned} \tau_{wx} &= A * \cos(\pi(y/2L_y)) * \sin(2\pi x/(Tc_w) - 2\pi t/T) & \text{for } |y| \leq L_y \\ \tau_{wx} &= 0 & \text{for } |y| > L_y \end{aligned}$$

where c_w is the phase speed of moving wind field, x is the zonal distance from a

reference longitude, y is the meridional distance from the equator, T is the period, A is the amplitude on the equator, and L_y ($=10^\circ$) is the meridional scale of wind field. The meridional wind stress is zero over the entire model domain. Figure 13a shows the zonal wind stress on the equator with $A=0.03$ N/m², $T=60$ days, and $c_w = 9$ m/s. These amplitude and phase speed are similar to those in surface wind anomalies east of the dateline associated with the MJO (e.g., Hendon and Salby 1994). Using this wind forcing, the model was first integrated from a state at rest for 250 days. This experiment is referred to as EX-LM-1 hereafter.

The SSH on the equator in EX-LM-1 from Day 50 to 230 is shown in Fig. 13b. Phase speeds of Kelvin waves between 165°W and 100°W are again estimated objectively as described in Appendix B. SSH fluctuations propagate eastward about 4 m/s, much faster than the 2.71 m/s phase speed of free Kelvin wave in this system. In most areas in the central and eastern Pacific, positive (negative) SSH anomalies are associated with westerly (easterly) winds. The westerly (easterly) wind stress along the trajectory of downwelling (upwelling) Kelvin waves generates an eastward (westward) zonal current anomaly. Since the wind stress moves faster than the free Kelvin wave speed, it continuously shifts the location of the maximum (minimum) SSH of Kelvin waves eastward. Hence the net effect of these zonal stresses along the wave trajectory is to increase the phase speed.

The model was also forced with the same wind field except the zonal wind stress is kept to be zero east of 170°W (Fig. 13c, referred to as EX-LM-2). The phase speed of SSH fluctuations in EX-LM-2 is then the free wave speed of ~ 2.7 m/s. The comparison between EX-LM-1 and EX-LM-2 also indicates that the wind stress in the eastern Pacific can also alter the amplitude of Kelvin waves, a possibility discussed in previous studies (e.g., Gill 1982, Hendon et al. 1998). While the amplitude of Kelvin wave is nearly the same along the trajectory east of the dateline in EX-LM-2, the

amplitude in the EX-LM-1 is enhanced as the Kelvin wave moves to around 150°W . The amplitude of waves decreases as the Kelvin wave propagates further east since the phase lag between wind stress and SSH becomes larger.

The model was then forced with the zonal wind stress in which the amplitude in the eastern Pacific changes in time (referred to as EX-LM-3). Figure 13e shows the zonal wind stress on the equator used in EX-LM-3. The wind stress is same as in EX-LM-1 until Day 90, then its amplitude east of 170°W linearly decreases to zero by Day 150. After Day 150, the the wind stress is the same as in EX-LM-2. Because of the variation of wind field in the eastern Pacific, the phase speeds of successive Kelvin waves progressively decrease with time (Fig. 13f) in a manner similar to that seen in observations and OCGM experiments.

Finally, the model was forced with daily wind stress anomalies used in the control experiment of OGCM. The model is integrated for 2 years from January 1, 2001. Figure 14 shows the intraseasonally filtered SSH and surface zonal current near the equator during the period encompassing the case study period during 2002. As in the OGCM, the linear model is able to simulate the systematic decrease of phase speed in time observed during this period (compare with Figs. 1 and 4).

While previous studies on forced Kelvin waves emphasize the changes of their amplitude by wind forcing (e.g., Hendon et al. 1998, Gill 1982), our OGCM and linear model experiments clearly demonstrate that propagating wind fields can also substantially alter the phase speed of a Kelvin wave. Based on the results of OGCM and linear model experiments, the observed systematic decrease of Kelvin wave phase speed can be explained as a continuous modification of free Kelvin waves by surface wind forcing in the eastern equatorial Pacific. Linear model experiments also eliminate nonlinearity as a major cause of these changes in phase speed.

5. Conclusions and discussion

Based on an analysis of the TAO mooring data, Roundy and Kiladis (2006) showed that there is often a systematic transient decrease in phase speeds of intraseasonal Kelvin waves associated with the MJO, leading to an increase in the period of waves toward the eastern part of the basin. This study examined the processes that might be responsible for this decrease in phase speed using OGCM and simple linear model experiments. A series of OGCM experiments forced with different surface wind stresses are designed to examine the effect of background currents and thermal structures of the upper ocean along with atmospheric forcing on Kelvin wave phase speed. In order to generate different upper ocean background states in each experiment, the model was first forced with different longer time scale (>100 days) wind stress while the intraseasonal component (20-100 days) of stress was kept the same in all experiments. The results indicate that the slowly varying upper ocean basic state is not the primary cause of changes in Kelvin wave phase speed identified in the TAO mooring data. The model is then integrated with wind stresses that include the intraseasonal component only in the western Pacific and exclude it in the central and eastern Pacific. These experiments demonstrate that the relatively weak time varying wind stress east of the dateline significantly affects the phase speed of Kelvin waves, which often results in a phase speed faster than the free wave speed. These faster waves contribute to systematic changes of phase speed evident in the TAO data. The results of OGCM experiments are further confirmed by experiments of a linear stratified model forced with an idealized wind stress, eliminating nonlinearity as a major contributing factor to the phase speed changes.

While this study identifies the mechanism by which Kelvin waves faster than the free wave speed are generated, RK06 also found Kelvin waves slower than the free

wave speed that also contribute to the decrease of phase speed in time. For example, during July 1997, the positive intraseasonal anomalies of dynamic height propagated eastward at $\sim 1.7\text{m/s}$, which is slower than the prior downwelling Kelvin wave observed in May (see Fig 11 in RK06). Although similar disturbances of SSH during this period are evident in the model output (not shown), the slow eastward propagation is not as clear as in the TAO data. RK06 speculated that these slower waves are the result of intraseasonal air-sea interaction associated with the MJO based on the phase relationships between SST, convection and dynamic height anomalies. The ability of the model experiments to simulate these slow Kelvin waves may be limited here by the exclusion of the important role of air-sea coupled processes in maintaining these waves. In addition, the NCEP winds may not be sufficiently accurate (Appendix A) to represent the required intraseasonal variability and amplification by air-sea feedback processes, since a small error in the phase relationship between the zonal wind and thermocline depth could result in a failure to sustain continued growth by air-sea coupling. Unlike these slower waves, this study indicates that the faster waves are simply the result of a forced upper ocean response, which may be the reason why the faster Kelvin waves are better simulated by the model.

The results of the present study along with those in RK06 suggest processes that could be partly responsible for the apparent discrepancy of dominant frequency between the MJO and associated Kelvin waves. The processes identified in this study and other mechanisms suggested in previous studies (Kessler et al. 1995, Hendon et al. 1998, see Section 1) are not mutually exclusive. The relative importance of each process in determining observed spectral characteristics of Kelvin waves likely depends on intraseasonal wind variability over the central and eastern Pacific that is generally weaker than that in the western Pacific, and which may vary from year to year. Hence data sets of accurate high frequency winds with fine spatial resolution in

this region, such as those from scatterometer instruments, will be crucial for further quantitative discussion of these processes.

Appendix A. Comparison of NCEP/NCAR reanalysis winds with in-situ and scatterometer measurements

Since this study examines equatorial Kelvin waves, the NCEP/NCAR reanalysis surface winds near the equator in the western Pacific (where the most Kelvin waves are generated) are compared with those from TOGA TAO and scatterometer measurements. The scatterometer data sets used in this study are derived from a space and time blend of NSCAT and QuikSCAT observations and the NCEP/NCAR reanalysis (Chin et al., 1998, Milliff et al. 1999, Milliff and Morzel 2001). Jiang et al (2005) also did a detailed comparison between TAO, QuikSCAT, and various analysis wind products, and overall our results compare well with theirs.

While the generation region of intraseasonal Kelvin waves varies somewhat from event to event, strong intraseasonal winds associated with large Kelvin waves are observed most frequently between 150°E - 180° near the equator (e.g., Hendon et al. 1998), and thus variations of average surface winds in this region are first compared. Figure 15a shows surface zonal winds (at 10m) in the western Pacific (147°E - 180°) near the equator from the NCEP/NCAR reanalysis, TOGA TAO buoys and NSCAT during 1996/97 when large intraseasonal variability of zonal winds associated with the MJO is observed. Zonal winds at 4m measured by TAO moorings are extrapolated to 10m using air temperature, specific humidity at 2m, and SST from the NCEP/NCAR reanalysis along with the TOGA COARE bulk flux algorithm (Fairall et al. 1995). Both intraseasonal and longer time scale variability measured by TAO moorings are well captured by the NCEP/NCAR reanalysis and NSCAT winds ($rr > 0.85$, Table 1).

The NCEP/NCAR reanalysis and scatterometer winds are also compared with TAO measurements during spring and summer 2002 when prominent phase speed changes of Kelvin waves were observed (Fig. 15b). Both NCEP and QSCAT zonal

winds are well correlated with TAO winds, indicating that reanalysis and scatterometer winds can capture intraseasonal variations in this region reasonably well. However, there are some discrepancies between the data sets in terms of the strength of intraseasonal winds during this period. For example, westerlies during late June and late July in QSCAT are stronger than those of TAO measurements, while westerlies during late May in the NCEP/NCAR reanalysis are weaker than those of TAO data. Similar discrepancies between scatterometer measurements and TAO data are evident during late May to June 1997 (Fig. 15a). Because of such discrepancies, there are significant rms differences in these datasets (Table 1). Since QSCAT winds tend to be stronger than those in TAO measurements over this region (Jiang et al. 2005), the rms difference between QSCAT and TAO data during this period is largely reduced when QSCAT is multiplied by a factor of 0.7 (Table 1). Note that the time series of TAO measurements in Fig. 15 might also have significant errors since the spatial coverage of the buoy is not as complete as in other data sets used to calculate an area average.

While there are occasional discrepancies in the amplitude of intraseasonal winds between these data sets, the NCEP winds in the western equatorial Pacific generally agree reasonably well with both in-situ and scatterometer measurements, and thus they are suitable for the present study. It should be noted that these comparisons of reanalysis and scatterometer data with TAO measurements in specific periods and locations do not provide evaluation of overall quality and reliability of these wind data sets (see Jiang et al. 2005). For example, synoptic scale wind variability might be better observed in the scatterometer data which could not be evaluated by the comparison with the TAO data. Nevertheless, these comparisons are useful for this particular study that discusses only a qualitative agreement of model simulations with observations during this period.

Appendix B. Estimate of phase speed

RK06 used both an automated objective scheme and subjective fitting to measure phase speeds using intraseasonally filtered dynamic height anomalies. Because of several difficulties, they have not developed a single objective method that can be applied for the entire period of their study. For example, the phase speed of an individual wave sometimes changes as it propagates eastward. Also, very often, it is difficult to objectively determine when and where the wave begins and ends. In this section, attempts are made to develop an objective scheme to measure the phase speed that can be applied to the period of spring and summer 2002 when the phase speed changes of Kelvin wave are particularly prominent.

The time series of dynamic height anomalies in the 20-100 day band from the TAO buoy at each station are first averaged over 2°N and 2°S . Then the local minima and maxima at each station along the Kelvin wave trajectory are plotted in a longitude-time diagram. A linear least squares fit is applied using these local maxima and minima in the diagram, and the phase speeds of downwelling and upwelling Kelvin waves are calculated from the slopes of these lines.

Figure 16 shows phase lines along with the local minima and maxima at each TAO station derived from the dynamic height data. The data from 7 stations for the upwelling Kelvin wave from late May to early July and the data from 6 stations for the subsequent downwelling Kelvin wave are used for the estimates based on the visual inspection of the beginning and the end of these waves. The phase speed estimates are close to the subjective estimate shown in Fig. 1. Examples of phase speed estimates using the model output will be shown in Appendix C.

Appendix C. Model results using different wind data

The comparison of different wind datasets in Appendix A shows that both NCEP and scatterometer winds can capture intraseasonal variability in the western equatorial Pacific reasonably well. However, the subtle differences in strength of the intraseasonal winds between different data sets may cause significant differences in ocean response. The sensitivity of the Kelvin wave response to different wind data sets is examined through additional model experiments.

The wind anomalies from QSCAT are first calculated by subtracting the climatological winds during January 2000-December 2005. Then these anomalies are added to the climatological winds calculated from the NCEP winds, and they are used to force the model. The model was integrated from 22 July 1999 with the initial condition derived from the control experiment at the same date. These procedures avoid a sudden change of the basic state at the beginning of this integration. Since intraseasonal winds from the scatterometer measurements are sometimes stronger than those in TAO observations (Table 1, Fig. 12b), another experiment which uses QSCAT wind anomalies multiplied by a factor 0.7 is also conducted.

Figure 17 shows interseasonally filtered SSH anomalies from these experiments during spring and summer 2002 along with those from the control experiment and dynamic height anomalies from TAO moorings. The phase speeds of Kelvin waves are measured as in Appendix B by identifying local maxima and minima at each 10° bin between 155°E and 125°W . The Kelvin waves in the experiment forced with QSCAT winds are much stronger than those observed by TAO measurements (Fig. 17a,b). These stronger waves may be caused partly by a combination of model deficiency and biases of the QSCAT winds. Using QSCAT winds multiplied by 0.7 significantly reduces the Kelvin wave amplitude, which becomes comparable to that in the TAO

data (Fig. 17c). Kelvin waves in the control experiment are weaker than those in TAO observations (Fig. 17d).

The phase speed of the downwelling Kelvin wave during July is slower than that of the prior upwelling Kelvin wave in all experiments. Also, the increase in period of these intraseasonal disturbances toward the east is evident in all experiments. However, there are quantitative differences in phase speed changes of these waves when the wave crests and troughs are used to measure the phase speed. The difference in phase speed between downwelling and upwelling Kelvin waves from mid-June to early August tends to be larger when the zonal wind anomalies and the amplitude of Kelvin waves are smaller. One interpretation for this difference in phase speed changes between the experiments is that the intraseasonal wind forcing east of the dateline could distort the Kelvin waves more efficiently when the amplitude of the waves is smaller. This interpretation is consistent with the phase speed of downwelling Kelvin waves during late May to early June. The phase speed of the downwelling Kelvin wave is faster than the subsequent upwelling Kelvin wave in the experiment with QSCAT winds, while it is slower in other two experiments. Since this downwelling Kelvin wave in the experiment with QSCAT winds is much stronger than the observed (Fig. 17b), the intraseasonal wind anomalies east of the dateline may not substantially influence the phase speed of this wave.

It should be noted that multiplying QSCAT wind anomalies by 0.7 is not necessarily the best way to examine the phase speed change in this study. We have also compared QSCAT zonal winds with those of TAO measurements in the eastern Pacific during spring and summer 2002, which shows that the strength of the intraseasonal winds agree very well (not shown). Hence multiplying 0.7 to wind anomalies causes significant errors of the intraseasonal winds east of the dateline which are shown to be important for the phase speed changes seen in the model (Section 4).

Acknowledgments

The TAO Project Office of NOAA/PMEL provided the mooring time series data. Constructive comments by two reviewers helped improve the original draft of this paper. Valuable discussions with Ralph Milliff on the scatterometer data are greatly appreciated. Weiqing Han and Jay McCreary provided us a code of the linear stratified model. We also would like to thank Alan Wallcraft for his assistance to run the HYCOM on the computing system at NOAA ESRL. This work was supported in part by a grant from the Computational and Information Systems Laboratory at NCAR. Toshiaki Shinoda is supported by NOAA CLIVAR-Pacific Grant from Office of Global Programs and NSF Grant OCE-0453046. Paul Roundy is supported by start-up funds from the Research Foundation for the State University of New York. George Kiladis is supported by NOAA's Climate Program Office under grant GC05-156.

References

- Benestad, R. E., R. T. Sutton, and D. L. T. Anderson, 2002: The effect of El Nino on intraseasonal Kelvin waves Q. J. R. Meteorol. Soc., 128, 1277-1291.
- Bergman, J. W., H. H. Hendon and K. M. Weickmann, 2001: Intraseasonal air-sea interaction at the onset of the 1997-98 El Nino. J. Climate, 14, 1702-1718.
- Bleck, R., 2002: An oceanic general circulation model framed in Hybrid Isopycnic-Cartesian Coordinates, Ocean Modelling, 4, 55-88.
- Chassignet, E. P., L. T. Smith, G. R. Halliwell, R. Bleck, 2003: North Atlantic simulations with Hybrid Coordinate Ocean Model (HYCOM): Impact of the vertical coordinate choice, reference density, and thermobaricity. J. Phys. Oceanogr., 33, 2504-2526.
- Cravatte, S., J. Picaut, and G. Eldin, 2003: Second and first baroclinic Kelvin modes in the equatorial Pacific at intraseasonal time scales. J. Geophys. Res. 108, 22: 1-20.
- Chin, T.M., R.F. Milliff, and W.G. Large, 1998: Basin-scale, high-wavenumber sea surface wind fields from a multiresolution analysis of scatterometer data. J. Atmos. Ocean. Tech., 15, 741-763.
- Enfield, D. B., 1987: The intraseasonal oscillation in eastern Pacific sea levels: How is it forced? J. Phys. Oceanogr., 17, 1860-1876.
- Fairall, C., E. F. Bradley, D. P. Rogers, J. B. Edson, and G. S. Young, 1996: The TOGA COARE bulk flux algorithm J. Geophys. Res., 101, 3747-3764.

- Fedorov, A. V., and W. K. Melville, 2000: Kelvin fronts on the equatorial thermocline. *J. Phys. Oceanogr.*, 30, 1692-1705
- Gill, A. E. 1982: *Atmosphere-Ocean Dynamics*. Academic Press, New York.
- Han, W., 2005: Origins and dynamics of the 90-day and 30-60 day variations in the equatorial Indian Ocean. *J. Phys. Oceanogr.* 708-728.
- Han, W, T. J. P. McCreary, D. L. T. Anderson, and A. J. Mariano, 1999: Dynamics of the eastward surface jets in the equatorial Indian Ocean. *J. Phys. Oceanogr.*, 29, 2191-2209.
- Han, W, T. Shinoda, L-L. Fu, and J. P. McCreary, 2006: Impact of atmospheric intraseasonal oscillations on the Indian Ocean dipole. *J. Phys. Oceanogr.*, 36, 670-690.
- Hendon, H. H., B. Leibmann, and J. Glick 1998: Oceanic Kelvin waves and Madden-Julian Oscillation. *J. Atmos. Sci.*, 55, 88-101.
- Hendon, H. H., and M. L. Salby, 1994: The life cycle of the Madden Julian oscillation. *J. Atmos. Sci.*, 51, 2225-2237.
- Jiang, C, M. F. Cronin, K. A. Kelly, and L. Thompson 2005: Evaluation of a hybrid satellite- and NWP-based turbulent heat flux product using Tropical Atmosphere-Ocean (TAO) buoys. *J. Geophys. Res.*, 110, C09007, doi:10.1029/2004JC002824.
- Johnson, E. S., and M. J. McPhaden, 1993: Structure of intraseasonal Kelvin waves in the equatorial Pacific Ocean. *J. Phys. Oceanogr.*, 23, 608-625.
- Kalnay, E., and Co-authors, 1996: The NCEP/NCAR 40-Year Reanalysis Project. *Bull. Amer. Meteor. Soc.*, 77, 437-471.

- Kessler, W. S., and R. Kleeman, 2000: Rectification of the Madden-Julian Oscillation into the ENSO cycle. *J. Climate.*, 13, 3560-3575.
- Kessler, W. S., M. J. McPhaden, and K. M. Weickmann, 1995: Forcing of intraseasonal Kelvin waves in the equatorial Pacific Ocean. *J. Geophys. Res.*, 100, 10613-10631.
- Large, W. G., and S. Pond, 1981: Open ocean momentum flux measurements in moderate to strong winds. *J. Phys. Oceanogr.*, 11, 324-336.
- Large, W. G., J. C. McWilliams and S. C. Doney, 1994: Oceanic vertical mixing: Review and a model with a nonlocal boundary layer parameterization. *Rev. Geophys.*, 32, 363-403.
- Lengaigne, M. J., P. Boulanger, C. Menkes, S. Masson, G. Madec, and P. Delecluse, 2002: Ocean response to the March 1997 westerly wind event. *J. Geophys. Res.*, 107(C12), 8015, doi:10.1029/2001JC000841.
- Levitus, S., R. Burgett, and T. P. Boyer, 1994:, *World Ocean Atlas Volume 3: Salinity*. NOAA Atlas, NESDIS 3, 99pp.
- Levitus, S., and T. P. Boyer, 1994:, *World Ocean Atlas Volume 4: Temperature*. NOAA Atlas, NESDIS 3, 117pp.
- Long, B., and P. Chang, 1990: Propagation of an equatorial Kelvin wave in a varying thermocline. *J. Phys. Oceanogr.*, 20, 1826-1841.
- Madden, R. A., and P. R. Julian, 1972: Description of global-scale circulation cells in the tropics with a 40-50 day period. *J. Atmos. Sci.*, 29, 1109-1123.
- Madden, R. A., and P. R. Julian, 1994: Observations of the 40-50 day tropical oscillation: a review. *Mon. Wea. Rev.*, 122, 814-837.

- Matsuno, T., 1966: Quasi-geostrophic motions in the equatorial area. *J. Meteor. Soc. Japan*, 44, 25-43.
- McCreary, J. P., 1980: Modeling wind-driven ocean circulation. Hawaii Institute of Geophysics Tech. Rep. HIG-80-3, 64 pp.
- McCreary, J. P., 1981: A linear stratified ocean model of the equatorial undercurrent. *Philos. Trans. Roy. Soc. London*, 298A, 603-635.
- McCreary, J. P., W. Han, D. Shanker, and S. R. Shetye, 1996: On the dynamics of the East India Coastal Current. Part 2: Numerical solutions. *J. Geophys. Res.*, 101, 113993-114010.
- McPhaden M. J., 1995: The Tropical Atmosphere-Ocean array is completed. *Bull. Amer. Meteorol. Soc.*, 76, 739-741.
- McPhaden M. J., 2002: Mixed layer temperature balance on intraseasonal timescales in the equatorial Pacific Ocean. *J. Climate*, 15, 2632-2647.
- McPhaden M. J., and B. A. Taft 1998: Dynamics of seasonal and intraseasonal variability in the eastern equatorial Pacific. *J. Phys. Oceanogr.*, 18, 1714-1732.
- McPhaden M. J., and X. Yu 1999: Equatorial waves and the 1997-98 El Nino. *Geophys. Res. Lett.*, 26, 2961-2964.
- Milliff, R.F., W.G. Large, J. Morzel, G. Danabasoglu, and T.M. Chin, 1999: Ocean general circulation model sensitivity to forcing from scatterometer winds. *J. of Geophys. Res.*, 104, 11337-11358.
- Milliff, R.F., and J. Morzel, 2001: The global distribution of the time-average wind stress curl from NSCAT. *J. Atmos. Sci.*, 58, 109-131.

- Moore, D. W., and S. G. H. Philander, 1977: Modeling of the tropical oceanic circulation. *The Sea*, Goldberg et al., Eds., Vol. 6, Interscience, 319-361.
- Philander, S. G. H., 1979: Equatorial waves in the presence of the equatorial undercurrent. *J. Phys. Oceanogr.*, 9, 254-262.
- Ralph, E. A., K. Bi, P. P. Niiler 1997: A Lagrangian description of the western equatorial Pacific response to the wind burst of December 1992. *J. Clim.*, 10, 1706-1721.
- Reynolds, R.W., N.A. Rayner, T.M. Smith, D.C. Stokes, and W. Wang, 2002: An improved in situ and satellite SST analysis for climate. *J. Climate*, 15, 1609-1625.
- Roundy, P. E., and G. N. Kiladis, 2006: Observed relationships between oceanic Kelvin waves and atmospheric forcing. *J Climate.*, 19, 5253-5272.
- Roundy, P. E., and G. N. Kiladis, 2007: Analysis of a reconstructed oceanic Kelvin wave dynamic height dataset for the period 1974-2005. *J Climate*. (in press) (available at <http://www.atmos.albany.edu/facstaff/roundy/rk2007.pdf>).
- Salby, M. L., and H. H. Hendon, 1994: Intraseasonal behavior of clouds, temperature, and convection in the Tropics. *J. Atmos. Sci.*, 51, 2207-2224.
- Serra, Y. L., M. F. Cronin, G. N. Kiladis 2007: Sub-seasonal variance of surface meteorological parameters in buoy observations and reanalyses. *Geophys. Res. Lett.*, 34, L12708, doi:10.1029/2007GL029506.
- Shaji, C., C. Wang, G. R. Halliwell Jr., A. Wallcraft, 2005: Simulation of tropical Pacific and Atlantic Oceans using a HYbrid Coordinate Ocean Model. *Ocean Modeling*, 9, 253-282.

- Shinoda, T., 2005: Impact of the diurnal cycle of solar radiation on intraseasonal SST variability in the western equatorial Pacific. *J. Climate*, 18, 2628-2636.
- Shinoda, T., and H. H. Hendon 1998: Mixed layer modeling of intraseasonal variability in the tropical western Pacific and Indian Oceans. *J. Climate*, 11, 2668-2685.
- Shinoda, T, and H. H. Hendon 2001: Upper ocean heat budget in response to the Madden Julian Oscillation in the western equatorial Pacific. *J. Climate*, 14, 4147-4165.
- Shinoda, T., H. H. Hendon and J. Glick 1998: Intraseasonal variability of surface fluxes and sea surface temperature in the tropical western Pacific and Indian Ocean. *J. Climate*, 11, 1685-1702.
- Shinoda, T, H. H. Hendon and J. Glick 1999: Intraseasonal surface fluxes in the tropical western Pacific and Indian Ocean from NCEP reanalyses. *Mon. Wea. Rev.*, 127, 678-693.
- Spillane, M. C., D. B. Enfield, and J. S. Allen, 1987: Intraseasonal oscillations in sea level along the west coast of the Americas. *J. Phys. Oceanogr.*, 99, 963-979.
- Waliser, D. E., R. Murtugudde, and L. Lucas, 2003: Indo-Pacific ocean response to atmospheric intraseasonal variability. Part I: Austral Summer and the Madden-Julian oscillation, *J. Geoph. Res. - Oceans*, 108, 3160, doi:10.1029/2002JC001620.
- Wheeler, M., and G. N. Kiladis, 1999: Convectively coupled equatorial waves: Analysis of clouds and temperature in the wavenumber-frequency domain. *J. Atmos. Sci.*, 56, 374-399.
- Zhang, C., 1996: Atmospheric intraseasonal variability at the surface in the tropical western Pacific Ocean. *J. Atmos. Sci.*, 53, 739-758.

Zhang, C., and J. Gottschalck, 2002: SST anomalies of ENSO and the Madden-Julian Oscillation in the Equatorial Pacific. *J. Climate*, 15, 2429-2445

Table 1: Correlation coefficients and rms difference between zonal winds from the NCEP/NCAR reanalysis, TAO moorings, NSCAT, and QSCAT in the area (147°E-180°E, 2°N-2°S), for the period 15 September 1996 - 30 June 1997, and 1 April - 15 August 2002

Variables	Correlation coefficient	Rms difference (m/s)
NCEP vs. TAO (1996-97)	0.86	1.36
NSCAT vs. TAO (1996-97)	0.87	1.37
NCEP vs. TAO (2002)	0.77	1.29
QSCAT vs. TAO (2002)	0.84	1.47
QSCATx0.7 vs. TAO (2002)	0.84	1.10

Figure captions

Figure 1: A longitude-time diagram of unfiltered (panel a) and 20-100 day filtered (panel b) dynamic height anomalies during April through August 2002 at the equator from the TOGA TAO data. The contour interval in panel b is 2 cm and the zero contour is omitted. Black lines are approximate trajectories of the filtered anomalies, and the corresponding phase speeds are shown in panel a. Longitude tick marks indicate TAO buoy locations. Adapted from Fig. 1 in Roundy and Kiladis (2006).

Figure 2: (a) Variations of the intensity of intraseasonal (20-100 day) sea surface height variability of the model (solid line) and dynamic height variability from the TAO data (dashed line) for the area 2°N - 2°S , 150°E - 110°W during December-April. Time series are normalized by their standard deviations, and the means are subtracted. The standard deviation of daily time series from the model is 0.57 cm and that from the TAO data is 0.74 cm. The means of time series are 1.85 cm (model) and 2.48 cm (TAO). (b) Correlation coefficients between daily intraseasonally filtered (20-100 day) time series of SSH from the model and dynamic height from the TAO data at each mooring stations along the equator for the period 1992-2004.

Figure 3: (a) A longitude-time diagram of intraseasonally (20-100 day) filtered dynamic height at the equator from the TAO data during December 1996-April 1997. The contour interval is 2 cm. The dashed contour lines indicate negative values. (b) A longitude-time diagram of intraseasonally (20-100 day) filtered SSH anomalies from the control experiments of OGCM. A 10° running mean is applied for the zonal direction.

Figure 4: (a) A longitude-time diagram of 20-100 day filtered SSH anomalies averaged over 2°N - 2°S from the control experiment during April-August, 2002. A 20° running mean is applied for the zonal direction. The contour interval is 0.5 cm with minimum contours at ± 0.5 cm. Areas where $\text{SSH} > 0.5$ cm are shaded. (b) Same as (a) except for the surface zonal velocity anomalies. The contour interval is 2.5 cm/s with minimum contours at ± 5 cm/s. Areas where the velocity > 5 cm/s are shaded.

Figure 5: (a) Time-depth cross sections of zonal velocity (cm/s) at the equator from 1 May through 10 September 2002 from the control experiment. (b) Same as (a) except for the 20-100 day filtered anomalies.

Figure 6: A longitude-time diagram of 100 day low pass filtered SSH averaged over 2°N - 2°S from EX-1 (left panel), EX-2 (middle panel), and EX-3 (right panel). The contour interval is 2 cm.

Figure 7: Zonal velocity at the depth of 20°C isotherm at the equator from EX-1 (left panel), EX-2 (middle panel), and EX-3 (right panel). The contour interval is 10 cm/s.

Figure 8: (a) Same as Fig. 4a except for EX-1. (b) Same as Fig. 4a except for EX-2. (c) Same as Fig. 4a except for EX-3.

Figure 9: (a) Same as Fig. 8c. (b) Daily zonal wind stress used in EX-3. The contour interval is 0.005 N/m^2 . The thick contour line indicates zero. (c) Same as (a) except for EX-4. (d) Same as (b) except for EX-4.

Figure 10: A longitude-time diagram of lag-regression composite of SSH (contours) and zonal wind stress (shading) from EX-1 (left panel) EX-3 (middle panel) and EX-4 (right panel). The interval of SSH contour is 0.25 cm, and the red (blue) line indicates positive (negative) values. The interval of wind stress shading is 0.001 N/m². Red and yellow shadings indicate positive values. Black lines are trajectories of filtered SSH anomalies and numbers near the lines are corresponding phase speeds.

Figure 11: Zonal wavenumber-frequency power spectra of SSH anomalies from the control experiment for the area 2°N-2°S east of 170°W. The base 10 logarithm is taken for plotting. The straight line indicates 2.7 m/s phase line. The curve in the negative wavenumber domain is the Rossby wave dispersion with the same equivalent depth of 2.7 m/s Kelvin wave.

Figure 12: (a) Zonal wavenumber-frequency power spectra of SSH anomalies from the EX-3 for the area 2°N-2°S east of 170°W. The base 10 logarithm is taken for plotting. The thick solid line indicates the 2.7 m/s phase line. The dashed line indicates the 5.0 m/s phase line. (b) Same as (a) except for EX-4.

Figure 13: (a) Zonal surface wind stress on the equator used in EX-LM-1. The contour interval is 0.005 N/m² with minimum contours at ± 0.005 N/m². Areas where SSH > 0.005 N/m² are shaded. The line is a trajectory of zonal wind stress and numbers near the line is the corresponding phase speed. (b) SSH on the equator from EX-LM-1. Lines are trajectories of the SSH and numbers near the lines are corresponding phase speeds. The contour interval is 1.0 cm with minimum contours at ± 1.0 cm. Areas where SSH > 1.0 cm are shaded. (c) Same as (a) except for EX-LM-2. (d) Same as (b) except for EX-LM-2. (e) Same as (a) except for EX-LM-3. (f) Same

as (b) except for EX-LM-3.

Figure 14: Same as Fig. 4 except for the linear model. The contour interval in (a) is 0.5 cm with minimum contours at ± 0.5 cm. Areas where $SSH > 0.5$ cm are shaded. The contour interval in (b) is 2 cm/s with minimum contours at ± 2 cm/s. Areas where $SSH > 2$ cm are shaded.

Figure 15: (a) Time series of zonal wind averaged over the area $2^{\circ}\text{N}-2^{\circ}\text{S}$, $147^{\circ}\text{E}-180^{\circ}$ from NSCAT (solid line), NCEP/NCAR reanalysis, (dashed line), and TAO moorings from 15 September 1996 to 30 June 1997. (b) Time series of zonal wind averaged over the area $2^{\circ}\text{N}-2^{\circ}\text{S}$, $147^{\circ}\text{E}-180^{\circ}$ from QSCAT (solid line), NCEP/NCAR reanalysis, (dashed line), and TAO moorings from 1 April to 15 August 2002.

Figure 16: Phase lines of local maxima and minima of 20-100 day filtered dynamic height anomalies from the TAO data. Circles indicate location of local maxima and minima at each TAO station.

Figure 17: (a) A longitude-time diagram of 20-100 day filtered dynamic height anomalies averaged over $2^{\circ}\text{N}-2^{\circ}\text{S}$ from the TAO data during 15 April-31 August, 2002. Lines are trajectories of filtered anomalies and numbers near the lines are corresponding phase speeds. The contour interval is 1.0 cm with minimum contours at ± 0.5 cm. Areas where $SSH > 1.5$ cm are shaded. (b) Same as (a) except for SSH anomalies from the model experiment forced with QSCAT wind anomalies. (c) Same as (a) except for SSH anomalies from the model experiment forced with QSCAT wind anomalies multiplied by 0.7. (d) Same as (a) except for SSH anomalies from the control experiment.

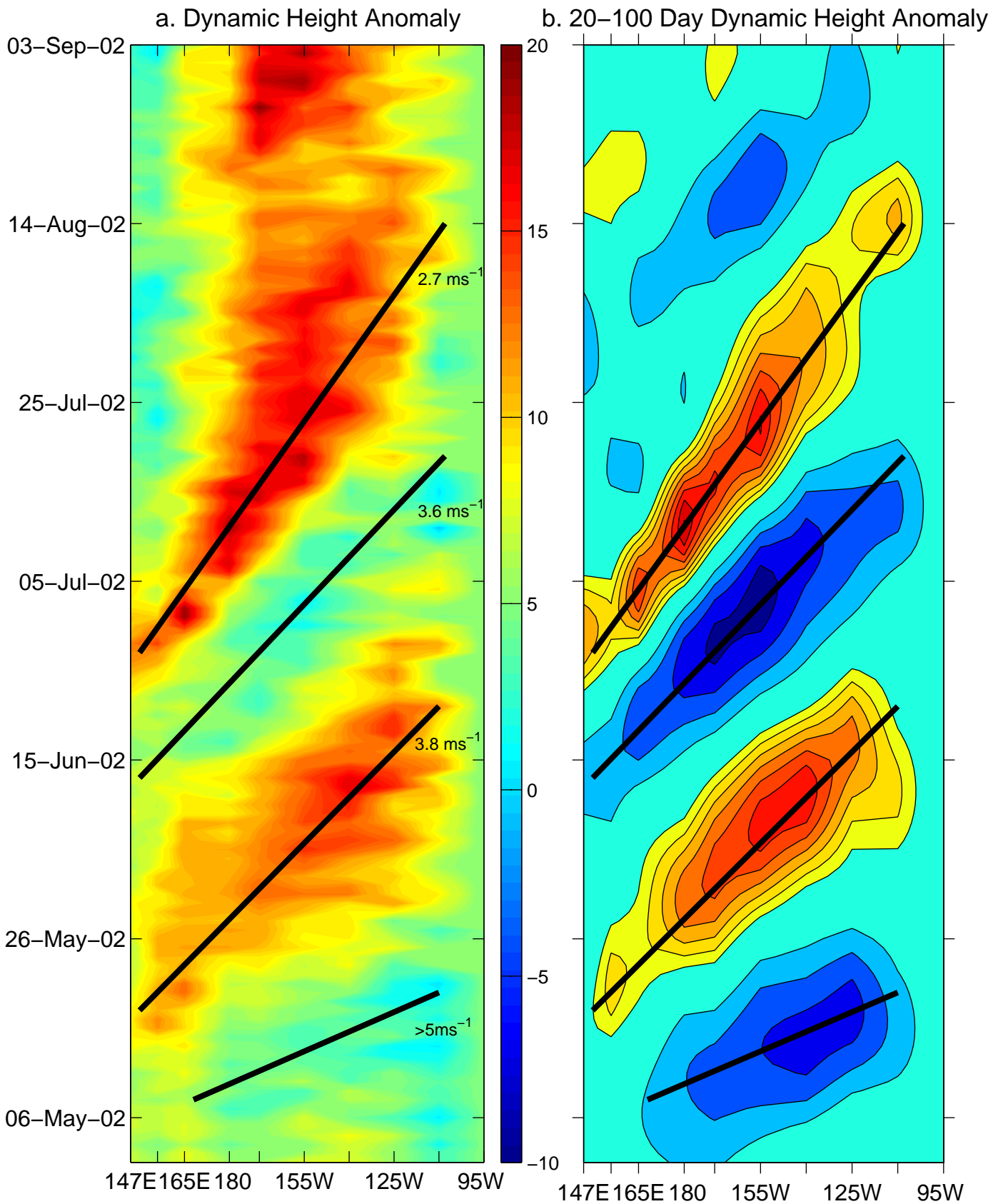


Figure 1: A longitude-time diagram of unfiltered (panel a) and 20-100 day filtered (panel b) dynamic height anomalies during April through August 2002 at the equator from the TOGA TAO data. The contour interval in panel b is 2 cm and the zero contour is omitted. Black lines are approximate trajectories of the filtered anomalies, and the corresponding phase speeds are shown in panel a. Longitude tick marks indicate TAO buoy locations. Adapted from Fig. 1 in Roundy and Kiladis (2006).

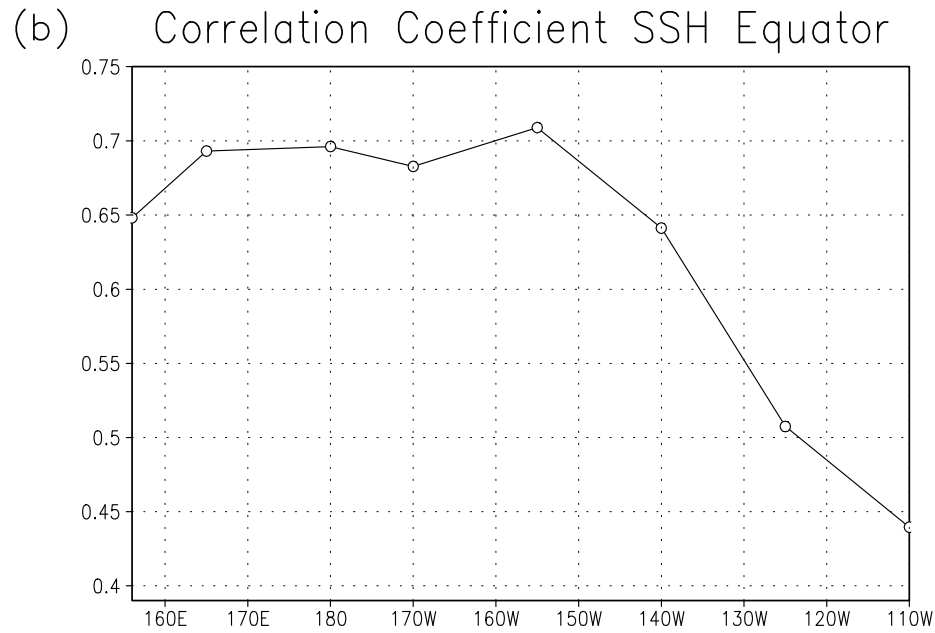
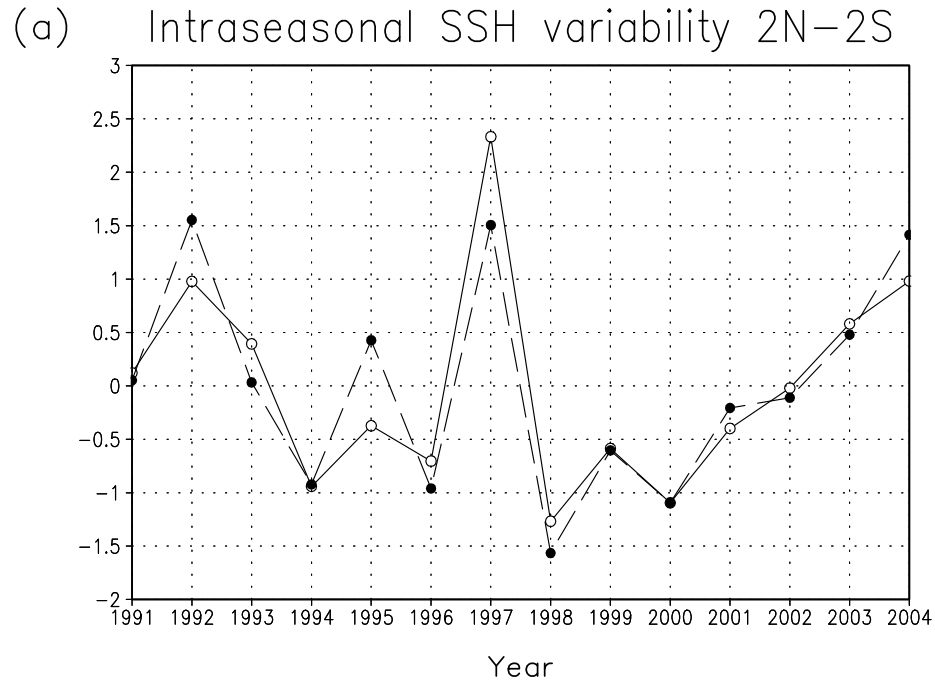


Figure 2: (a) Variations of the intensity of intraseasonal (20-100 day) sea surface height variability of the model (solid line) and dynamic height variability from the TAO data (dashed line) for the area 2°N-2°S, 150°E-110°W during December-April. Time series are normalized by their standard deviations, and the means are subtracted. The standard deviation of daily time series from the model is 0.57 cm and that from the TAO data is 0.74 cm. The means of time series are 1.85 cm (model) and 2.48 cm (TAO). (b) Correlation coefficients between daily intraseasonally filtered (20-100 day) time series of SSH from the model and dynamic height from the TAO data at each mooring stations along the equator for the period 1992-2004.

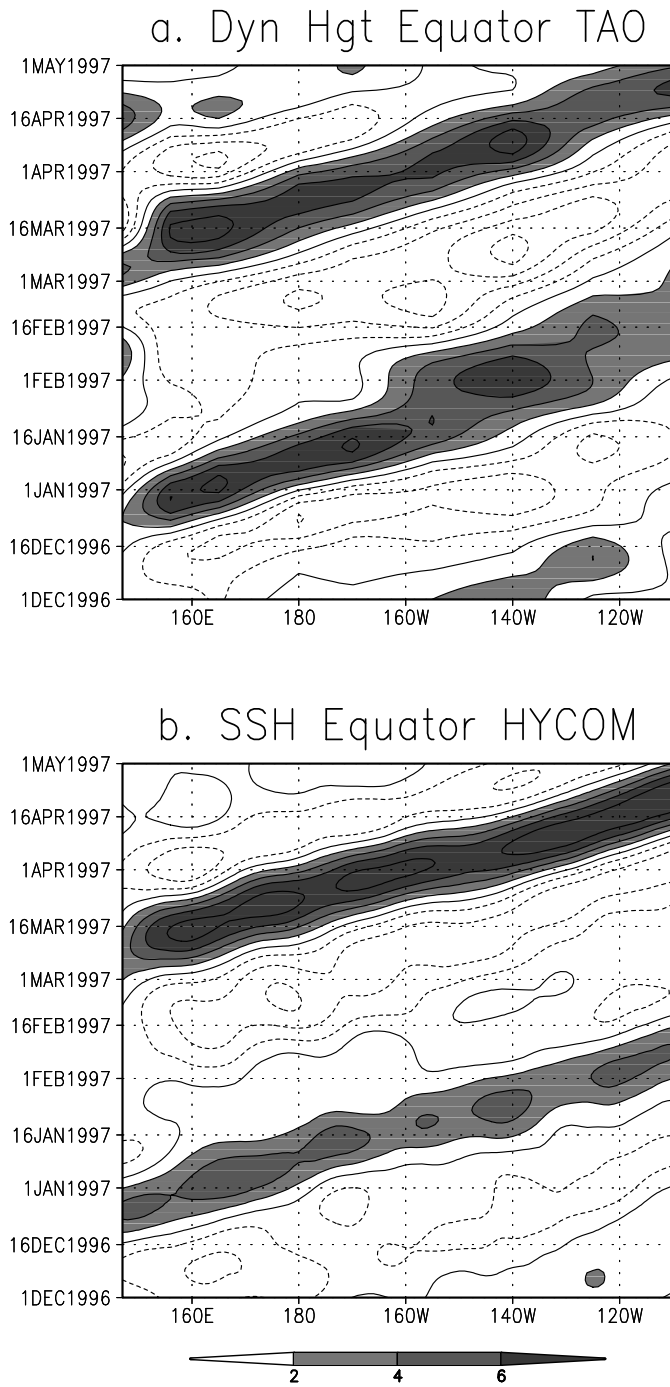


Figure 3: (a) A longitude-time diagram of intraseasonally (20-100 day) filtered dynamic height at the equator from the TAO data during December 1996-April 1997. The contour interval is 2 cm. The dashed contour lines indicate negative values. (b) A longitude-time diagram of intraseasonally (20-100 day) filtered SSH anomalies from the control experiments of OGCM. A 10° running mean is applied for the zonal direction.

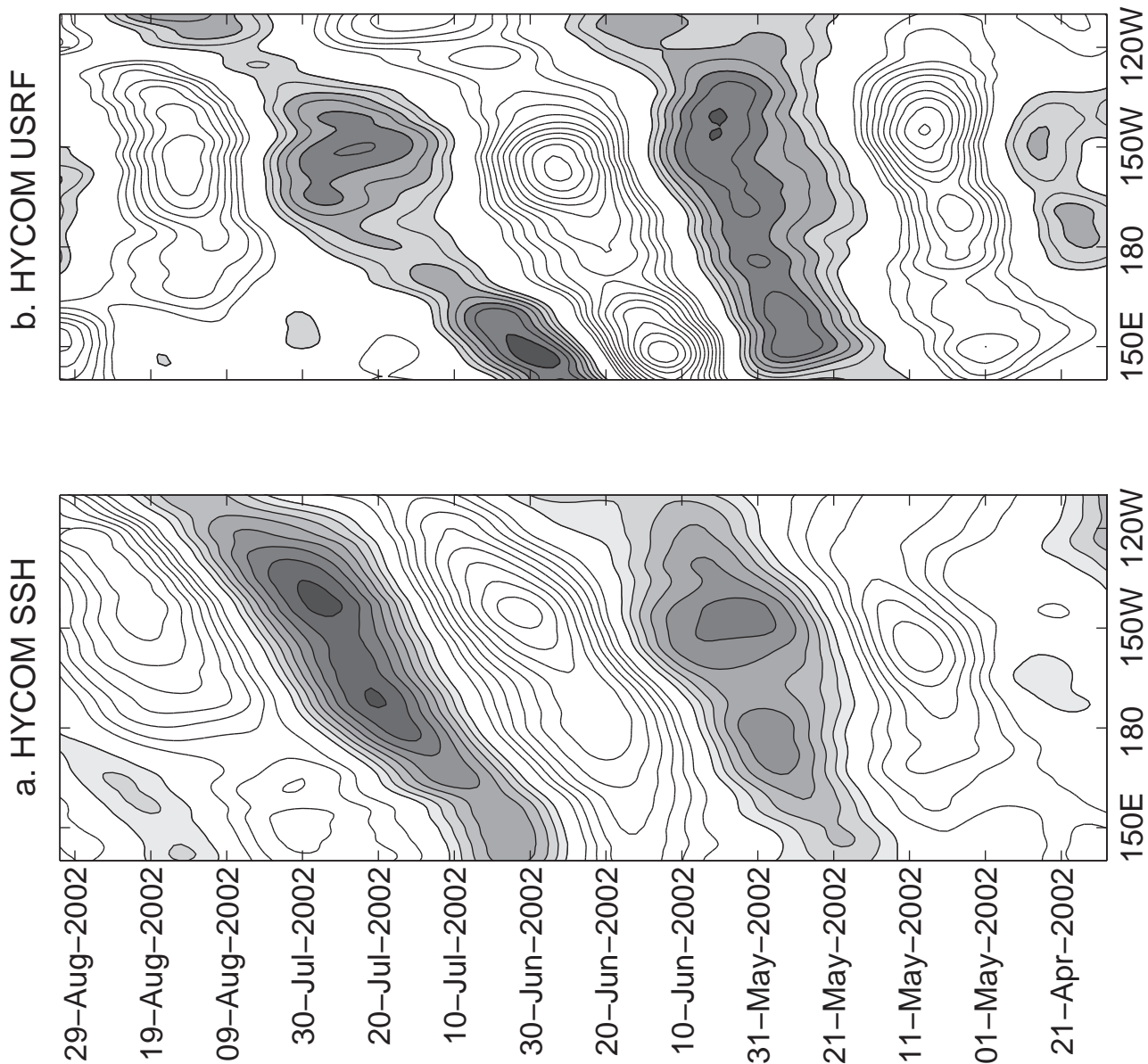


Figure 4: (a) A longitude-time diagram of 20-100 day filtered SSH anomalies averaged over 2°N - 2°S from the control experiment during April-August, 2002. A 20° running mean is applied for the zonal direction. The contour interval is 0.5 cm with minimum contours at ± 0.5 cm. Areas where $\text{SSH} > 0.5$ cm are shaded. (b) Same as (a) except for the surface zonal velocity anomalies. The contour interval is 2.5 cm/s with minimum contours at ± 5 cm/s. Areas where the velocity > 5 cm/s are shaded.

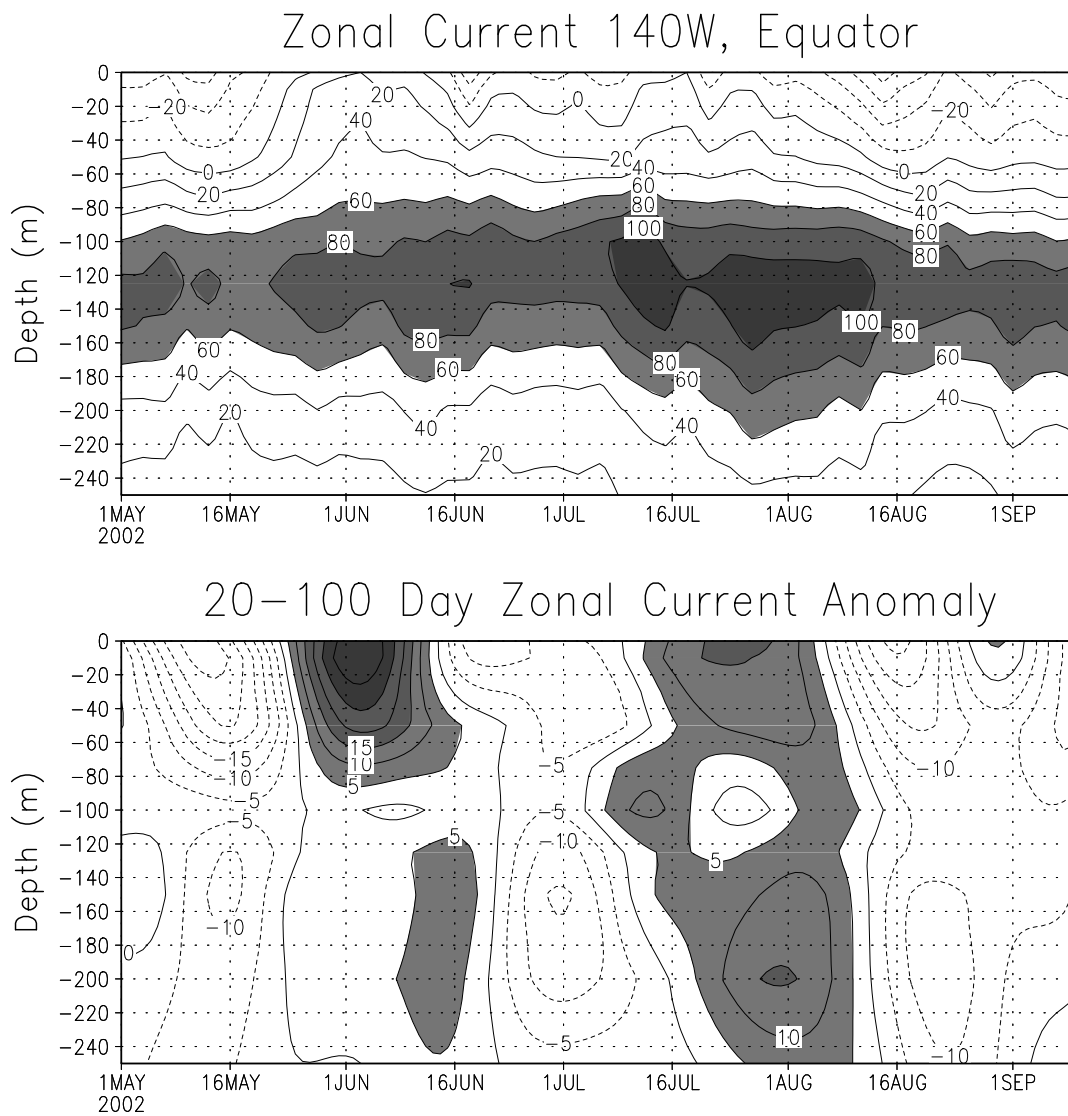


Figure 5: (a) Time-depth cross sections of zonal velocity (cm/s) at the equator from 1 May through 10 September 2002 from the control experiment. (b) Same as (a) except for the 20-100 day filtered anomalies.

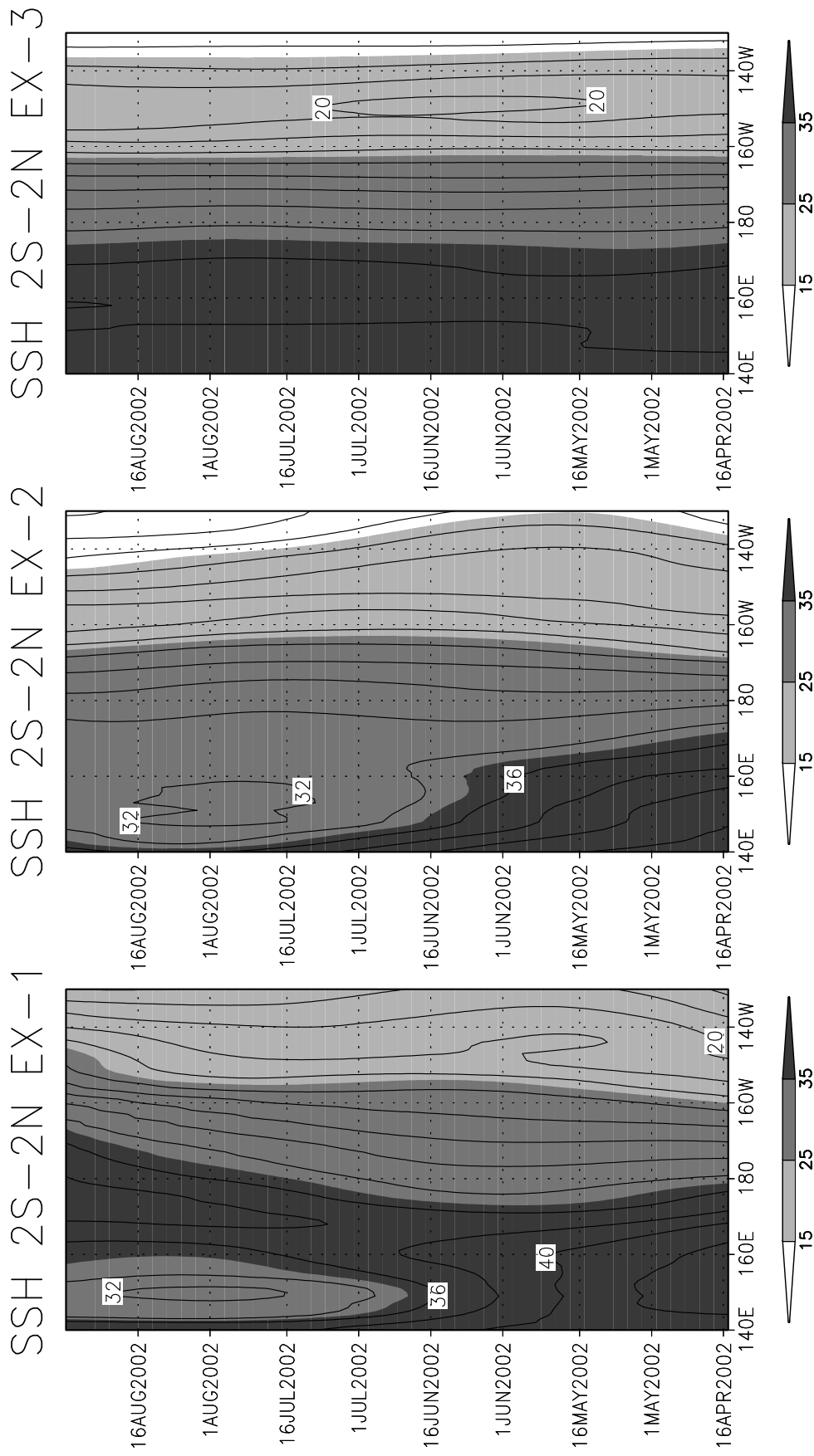


Figure 6: A longitude-time diagram of 100 day low pass filtered SSH averaged over 2°N-2°S from EX-1 (left panel), EX-2 (middle panel), and EX-3 (right panel). The contour interval is 2 cm.

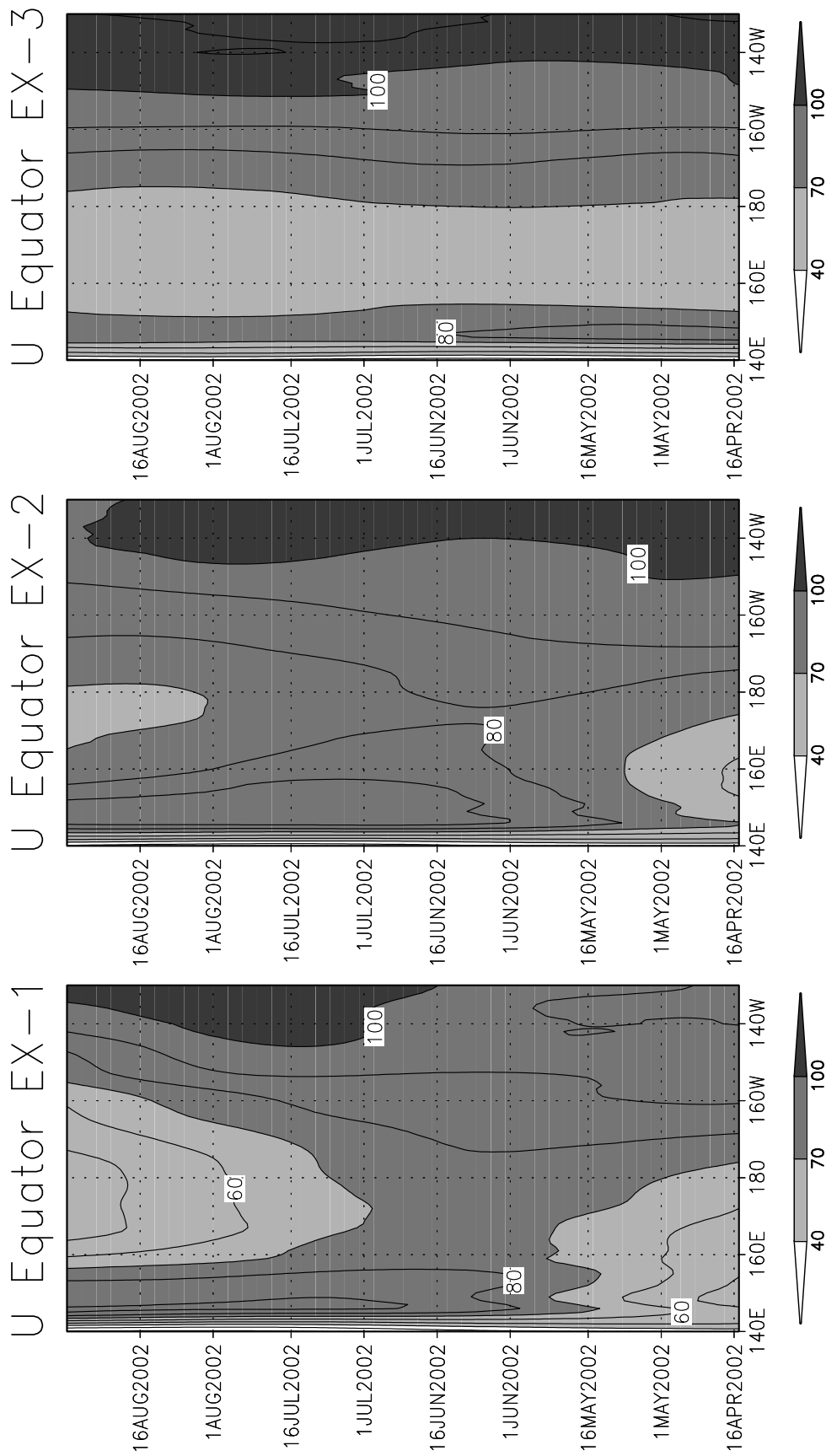


Figure 7: Zonal velocity at the depth of 20°C isotherm at the equator from EX-1 (left panel), EX-2 (middle panel), and EX-3 (right panel). The contour interval is 10 cm/s.

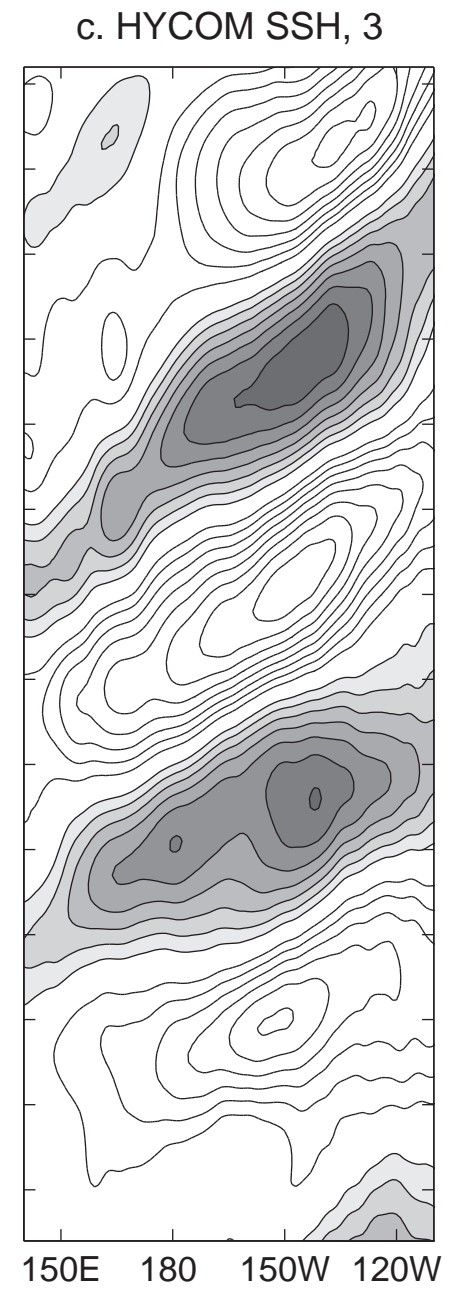
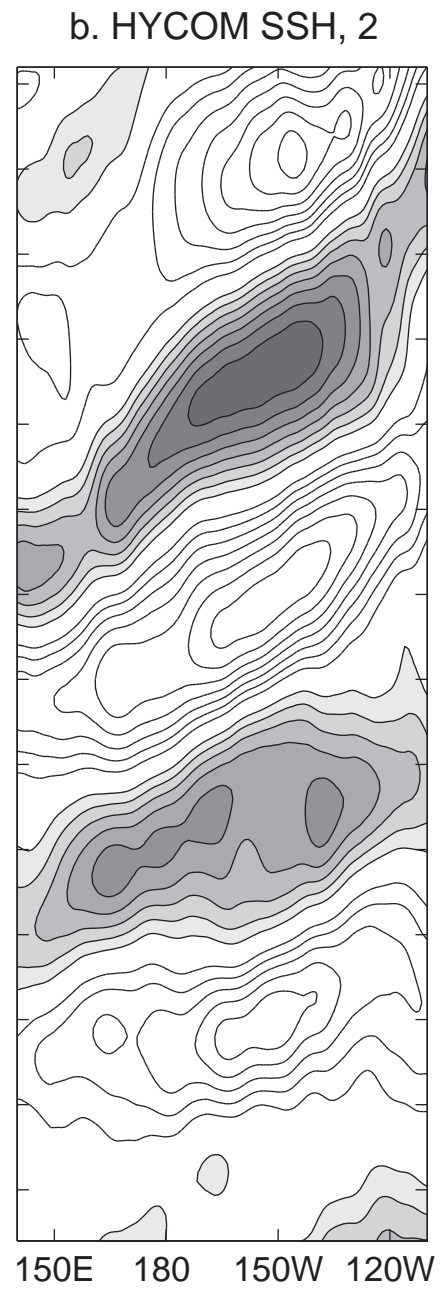
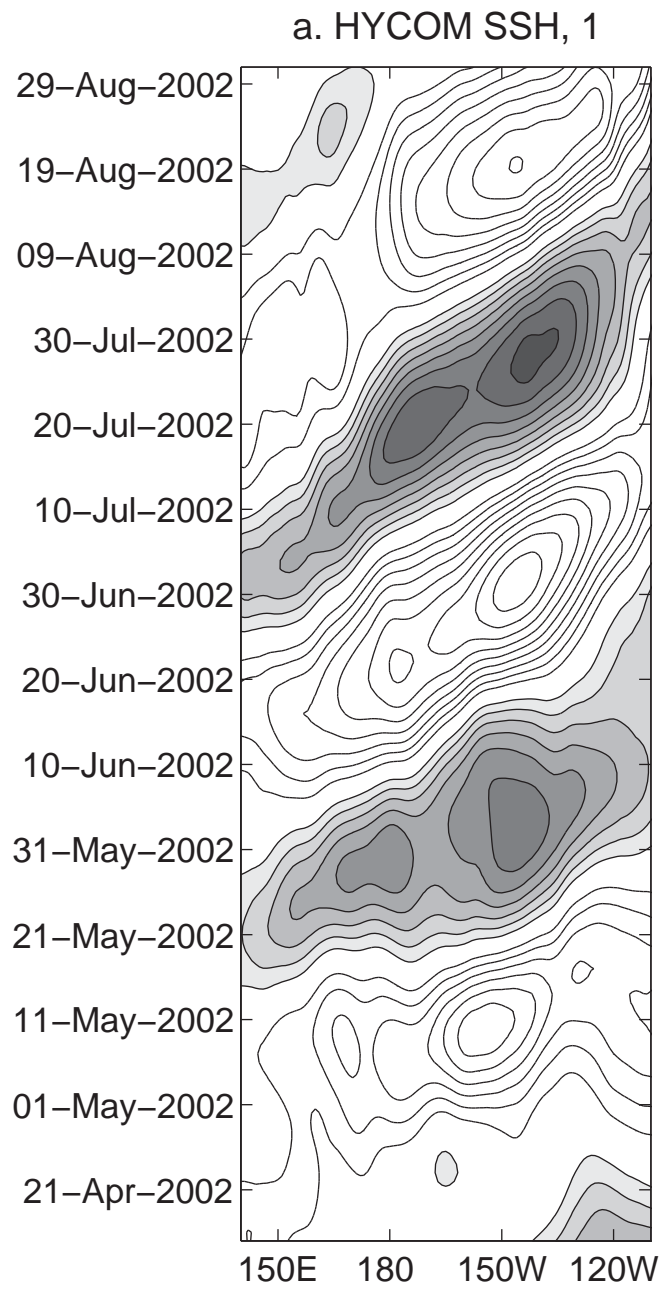
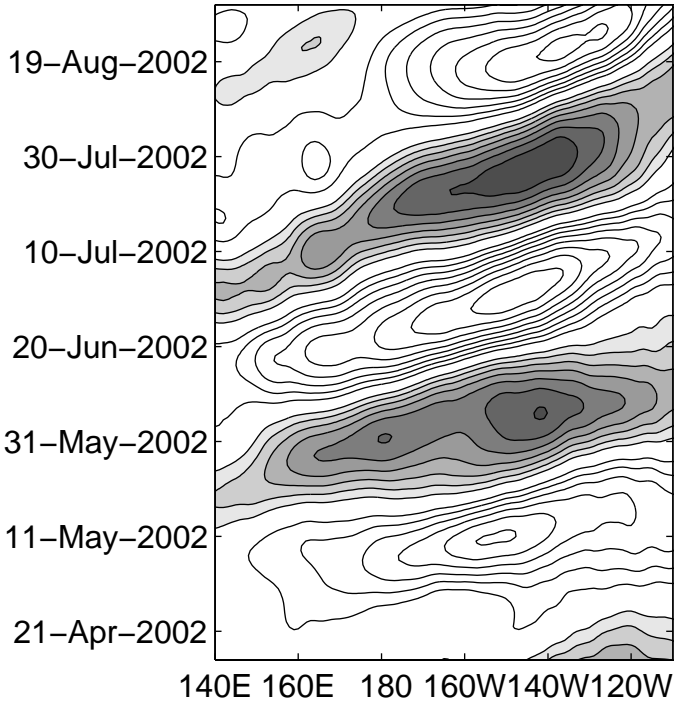
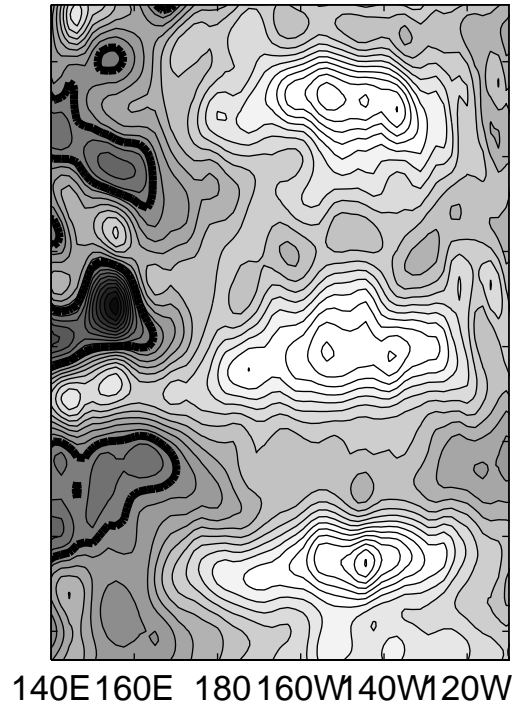


Figure 8: (a) Same as Fig. 4a except for EX-1. (b) Same as Fig. 4a except for EX-2.
(c) Same as Fig. 4a except for EX-3.

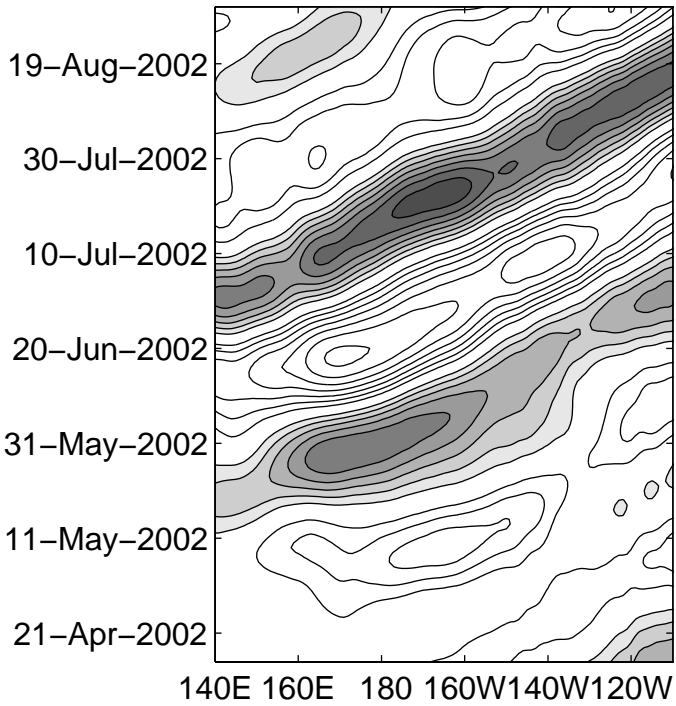
a. HYCOM SSH, Exp 3



b. HYCOM Tau, Exp 3



c. HYCOM SSH, Exp 4



d. HYCOM Tau, Exp 4

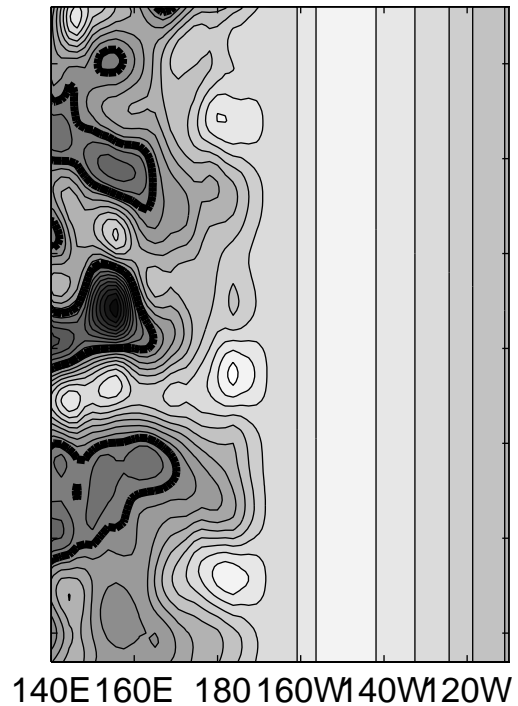


Figure 9: (a) Same as Fig. 8c. (b) Daily zonal wind stress used in EX-3. The contour interval is 0.005 N/m^2 . The thick contour line indicates zero. (c) Same as (a) except for EX-4. (d) Same as (b) except for EX-4.

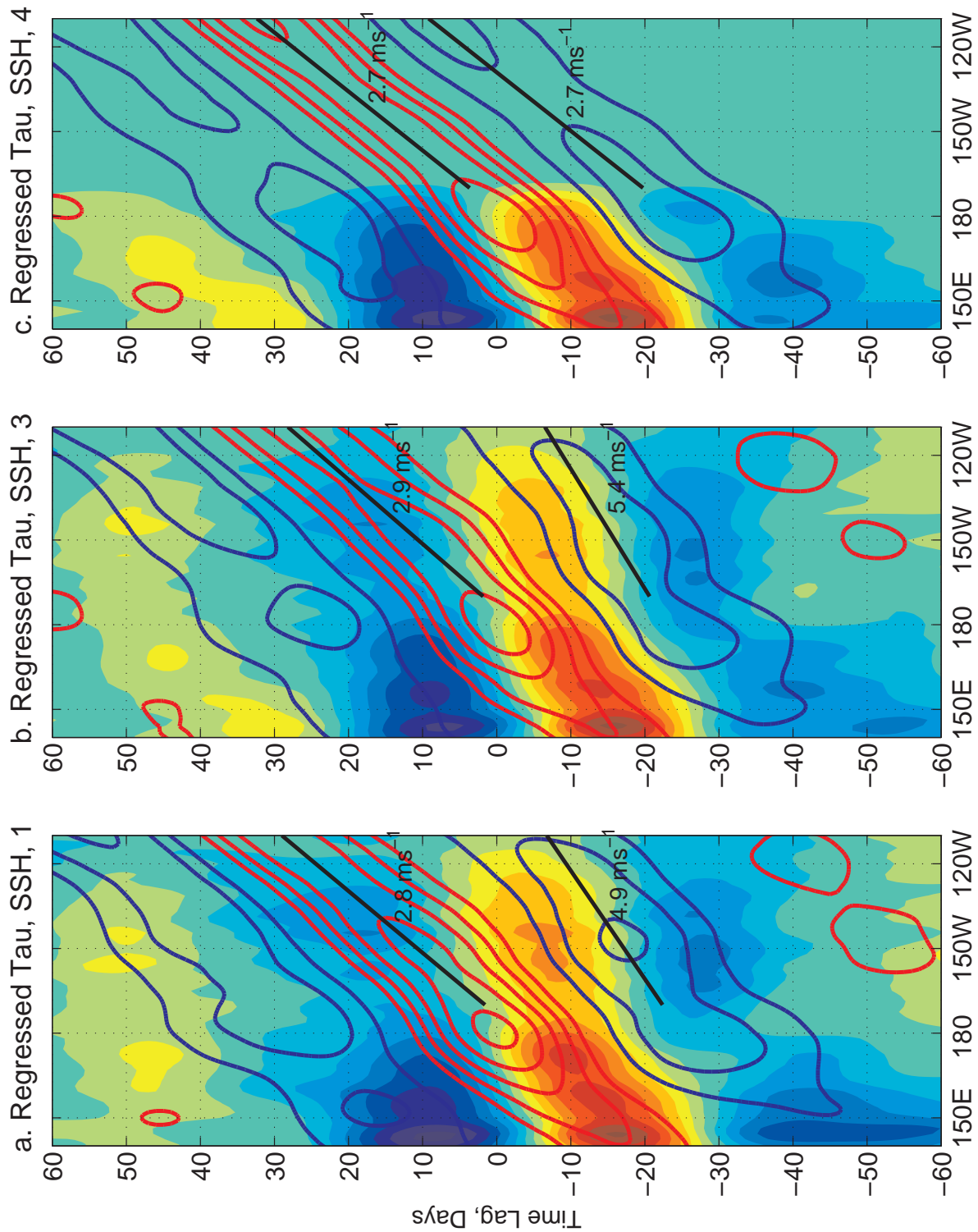


Figure 10: A longitude-time diagram of lag-regression composite of SSH (contours) and zonal wind stress (shading) from EX-1 (left panel) EX-3 (middle panel) and EX-4 (right panel). The interval of SSH contour is 0.25 cm, and the red (blue) line indicates positive (negative) values. The interval of wind stress shading is 0.001 N/m^2 . Red and yellow shadings indicate positive values. Black lines are trajectories of filtered SSH anomalies and numbers near the lines are corresponding phase speeds.

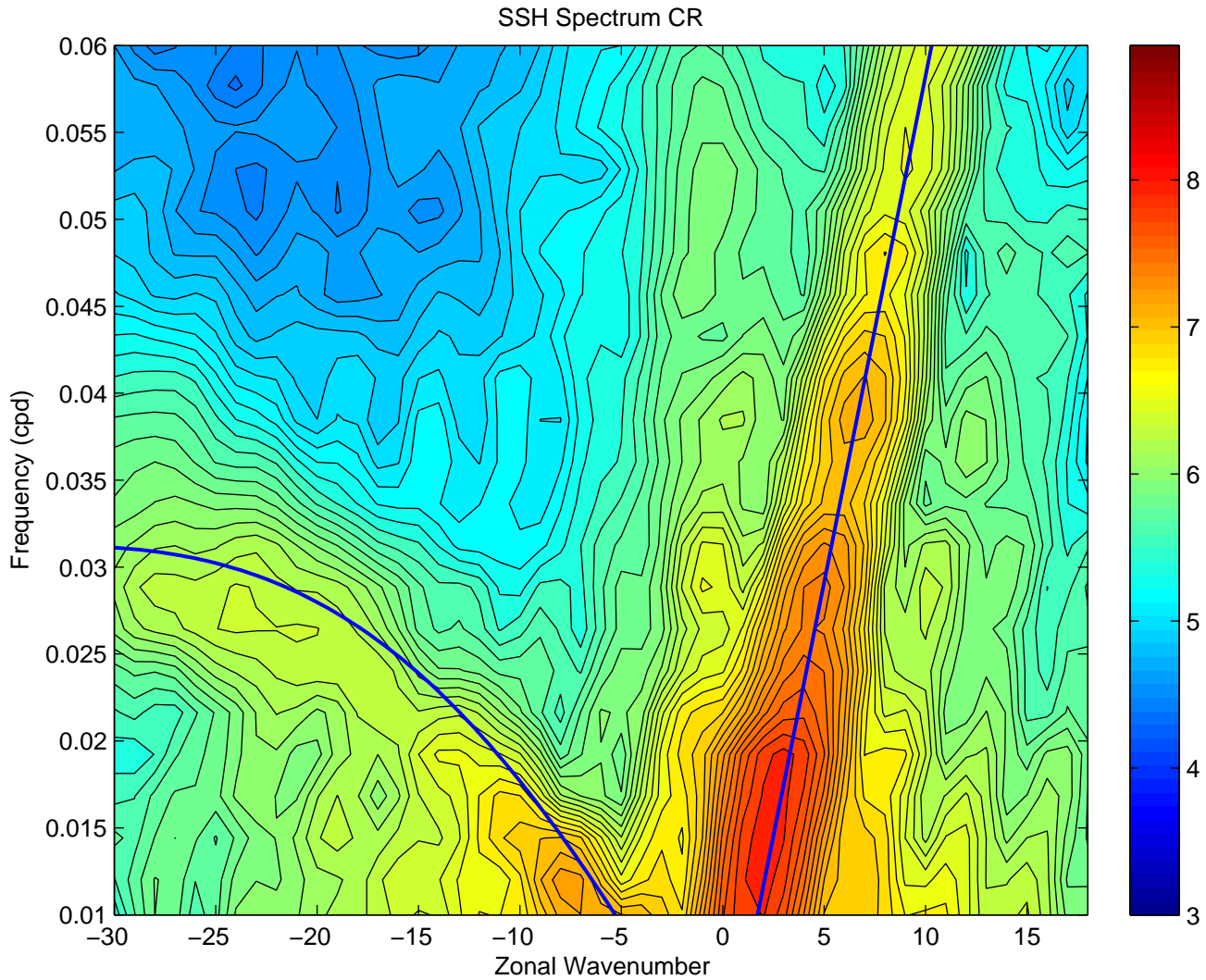


Figure 11: Zonal wavenumber-frequency power spectra of SSH anomalies from the control experiment for the area 2°N - 2°S east of 170°W . The base 10 logarithm is taken for plotting. The straight line indicates 2.7 m/s phase line. The curve in the negative wavenumber domain is the Rossby wave dispersion with the same equivalent depth of 2.7 m/s Kelvin wave.

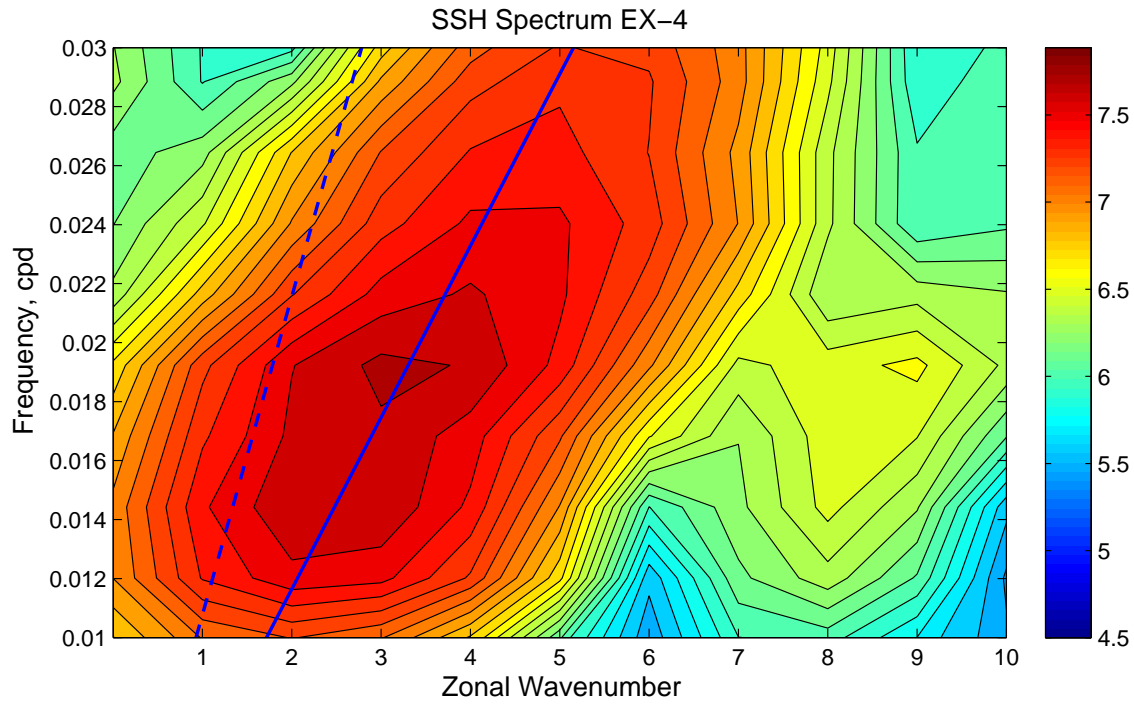
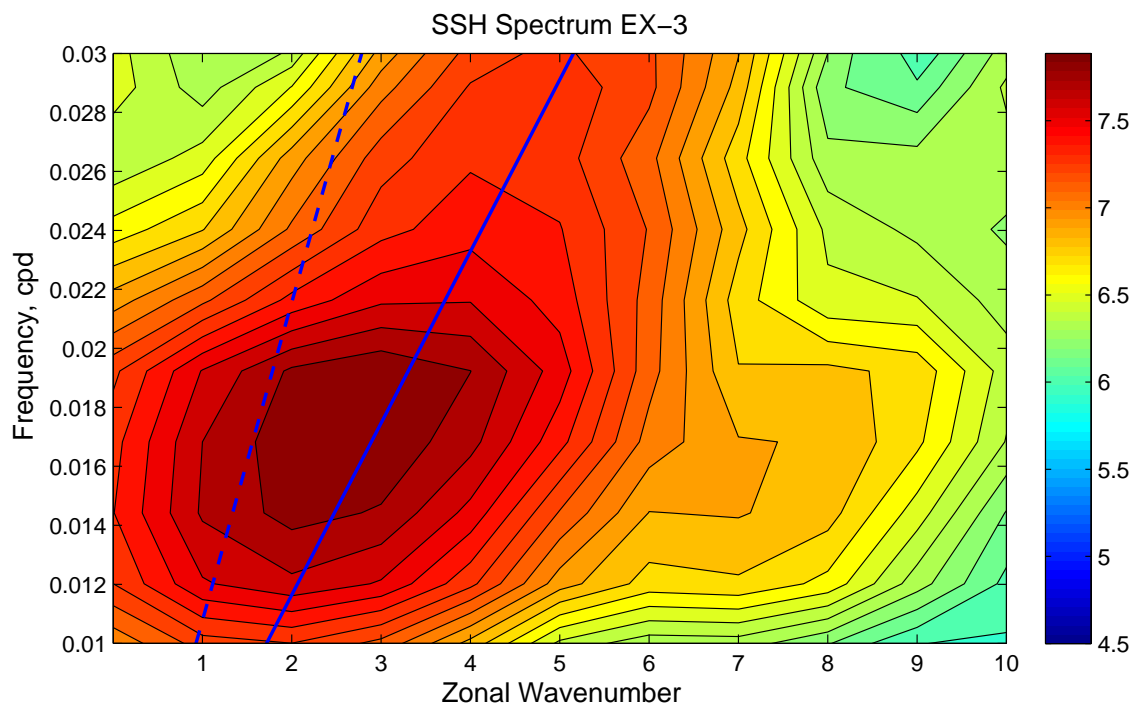


Figure 12: (a) Zonal wavenumber-frequency power spectra of SSH anomalies from the EX-3 for the area 2°N-2°S east of 170°W. The base 10 logarithm is taken for plotting. The thick solid line indicates the 2.7 m/s phase line. The dashed line indicates the 5.0 m/s phase line. (b) Same as (a) except for EX-4.

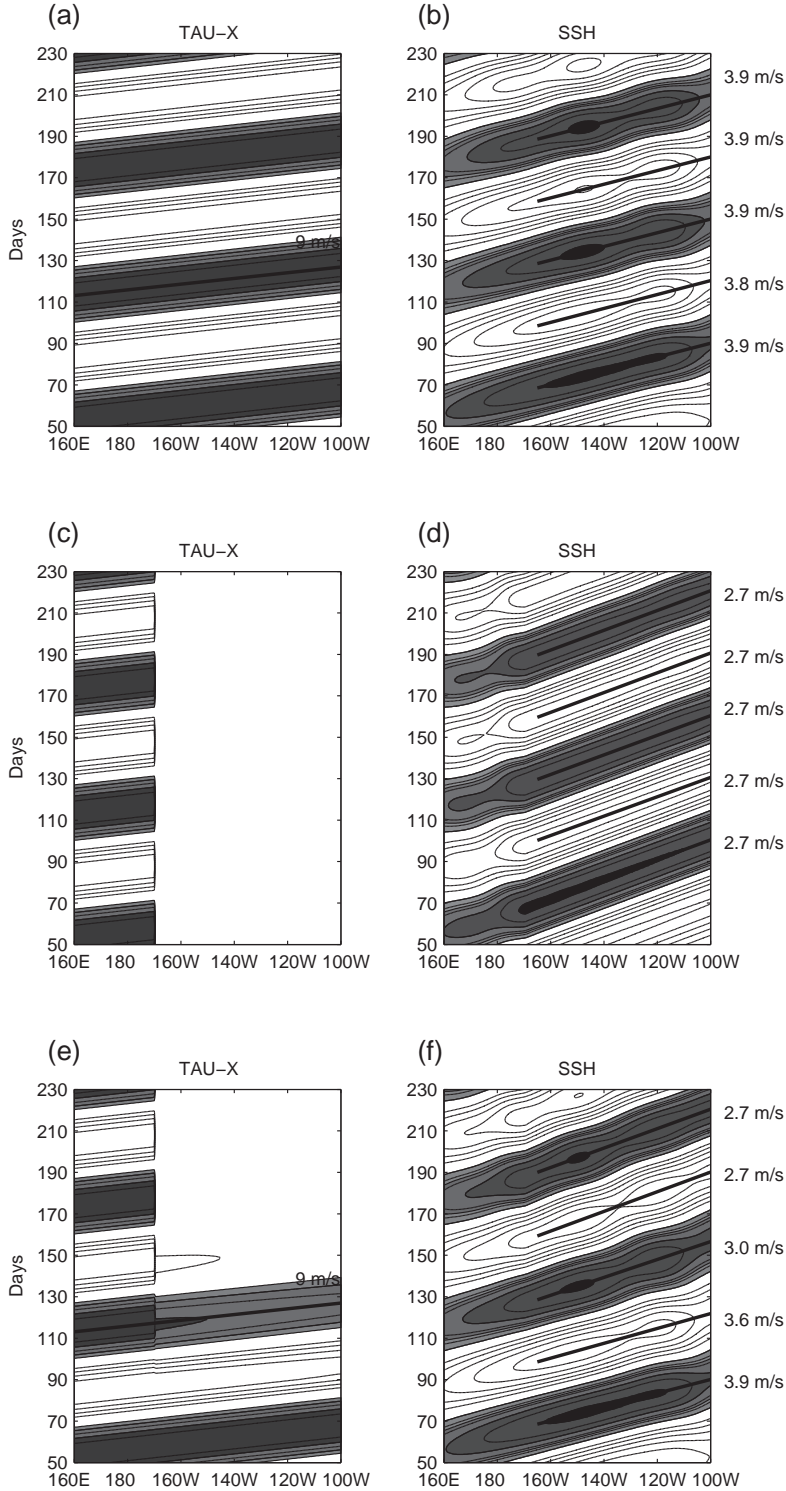
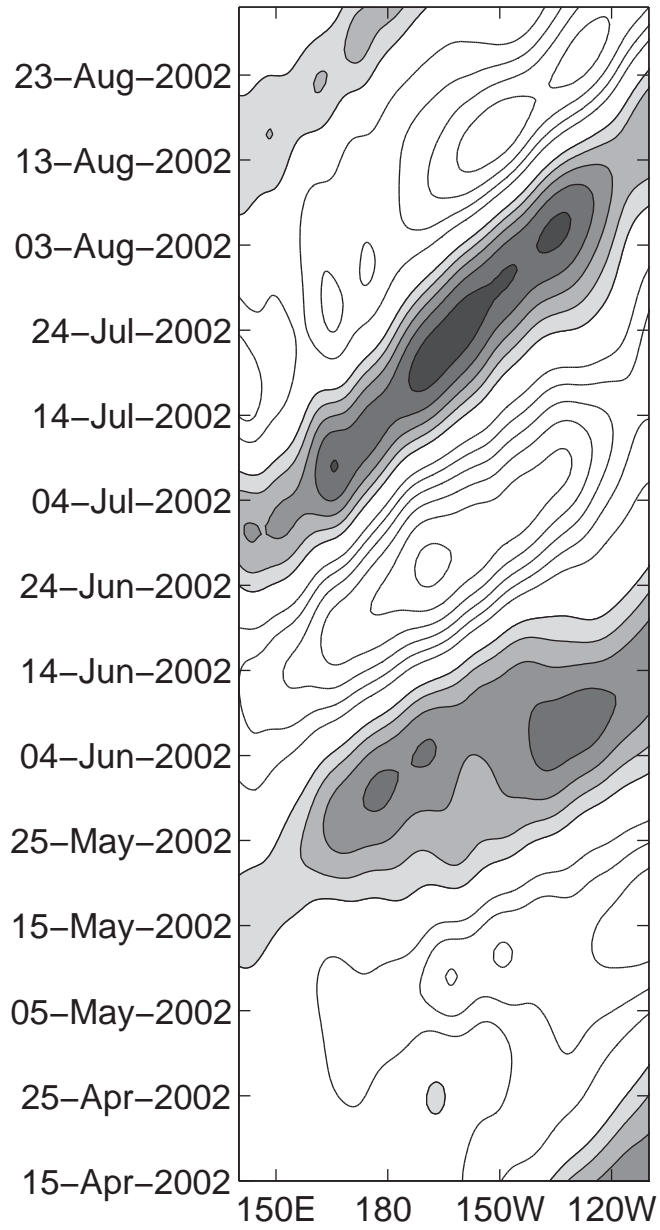


Figure 13: (a) Zonal surface wind stress on the equator used in EX-LM-1. The contour interval is 0.005 N/m^2 with minimum contours at $\pm 0.005 \text{ N/m}^2$. Areas where $\text{SSH} > 0.005 \text{ N/m}^2$ are shaded. The line is a trajectory of zonal wind stress and numbers near the line is the corresponding phase speed. (b) SSH on the equator from EX-LM-1. Lines are trajectories of the SSH and numbers near the lines are corresponding phase speeds. The contour interval is 1.0 cm with minimum contours at $\pm 1.0 \text{ cm}$. Areas where $\text{SSH} > 1.0 \text{ cm}$ are shaded. (c) Same as (a) except for EX-LM-2. (d) Same as (b) except for EX-LM-2. (e) Same as (a) except for EX-LM-3. (f) Same as (b) except for EX-LM-3.

a. LM SSH



b. LM USRF

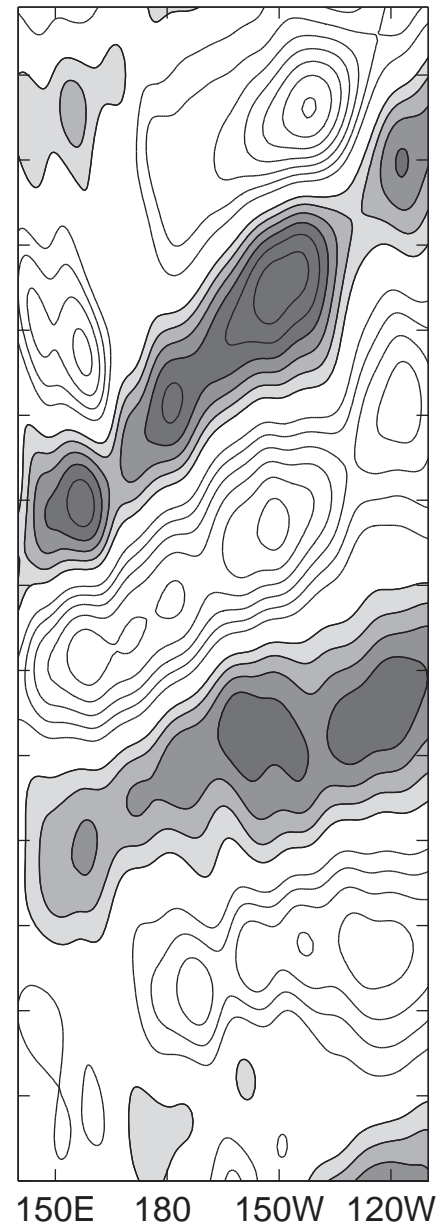


Figure 14: Same as Fig. 4 except for the linear model. The contour interval in (a) is 0.5 cm with minimum contours at ± 0.5 cm. Areas where SSH > 0.5 cm are shaded. The contour interval in (b) is 2 cm/s with minimum contours at ± 2 cm/s. Areas where SSH > 2 cm are shaded.

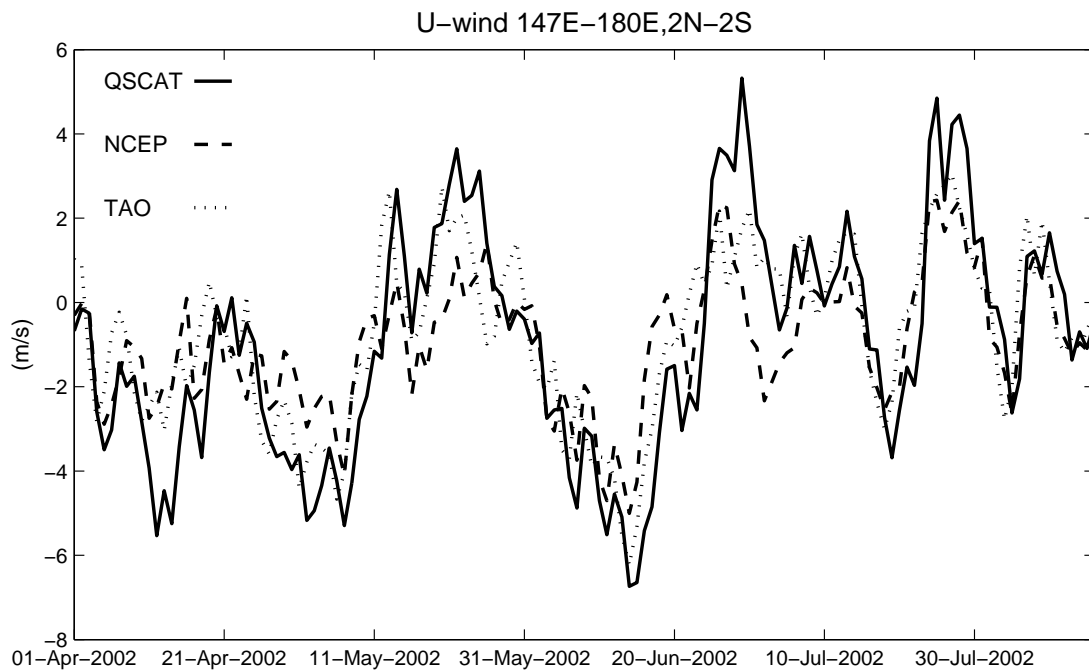
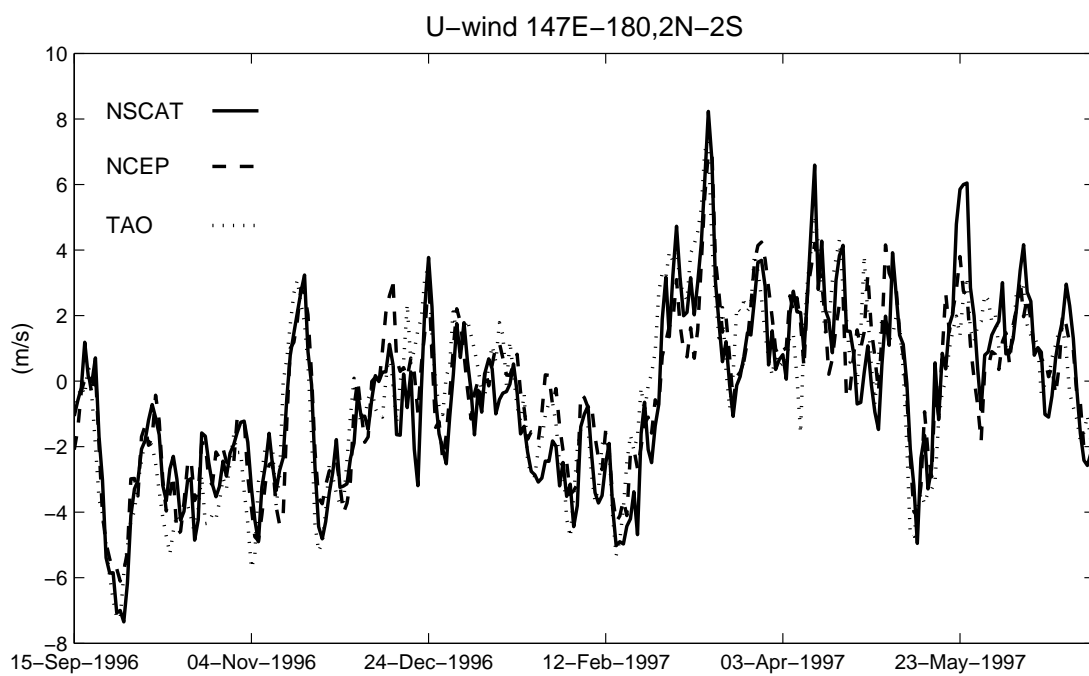


Figure 15: (a) Time series of zonal wind averaged over the area 2°N - 2°S , 147°E - 180° from NSCAT (solid line), NCEP/NCAR reanalysis, (dashed line), and TAO moorings from 15 September 1996 to 30 June 1997. (b) Time series of zonal wind averaged over the area 2°N - 2°S , 147°E - 180° from QSCAT (solid line), NCEP/NCAR reanalysis, (dashed line), and TAO moorings from 1 April to 15 August 2002.

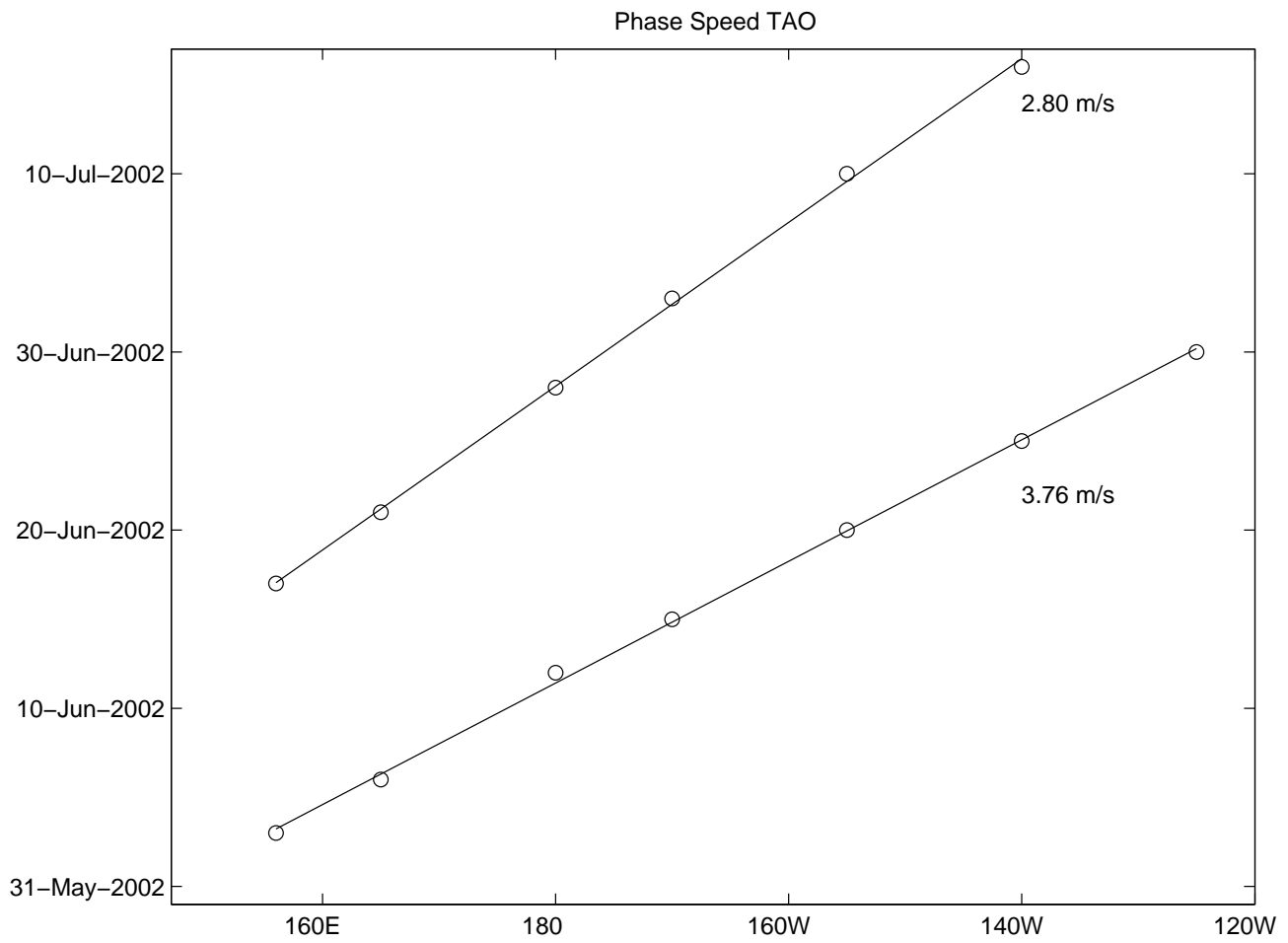


Figure 16: Phase lines of local maxima and minima of 20-100 day filtered dynamic height anomalies from the TAO data. Circles indicate location of local maxima and minima at each TAO station.

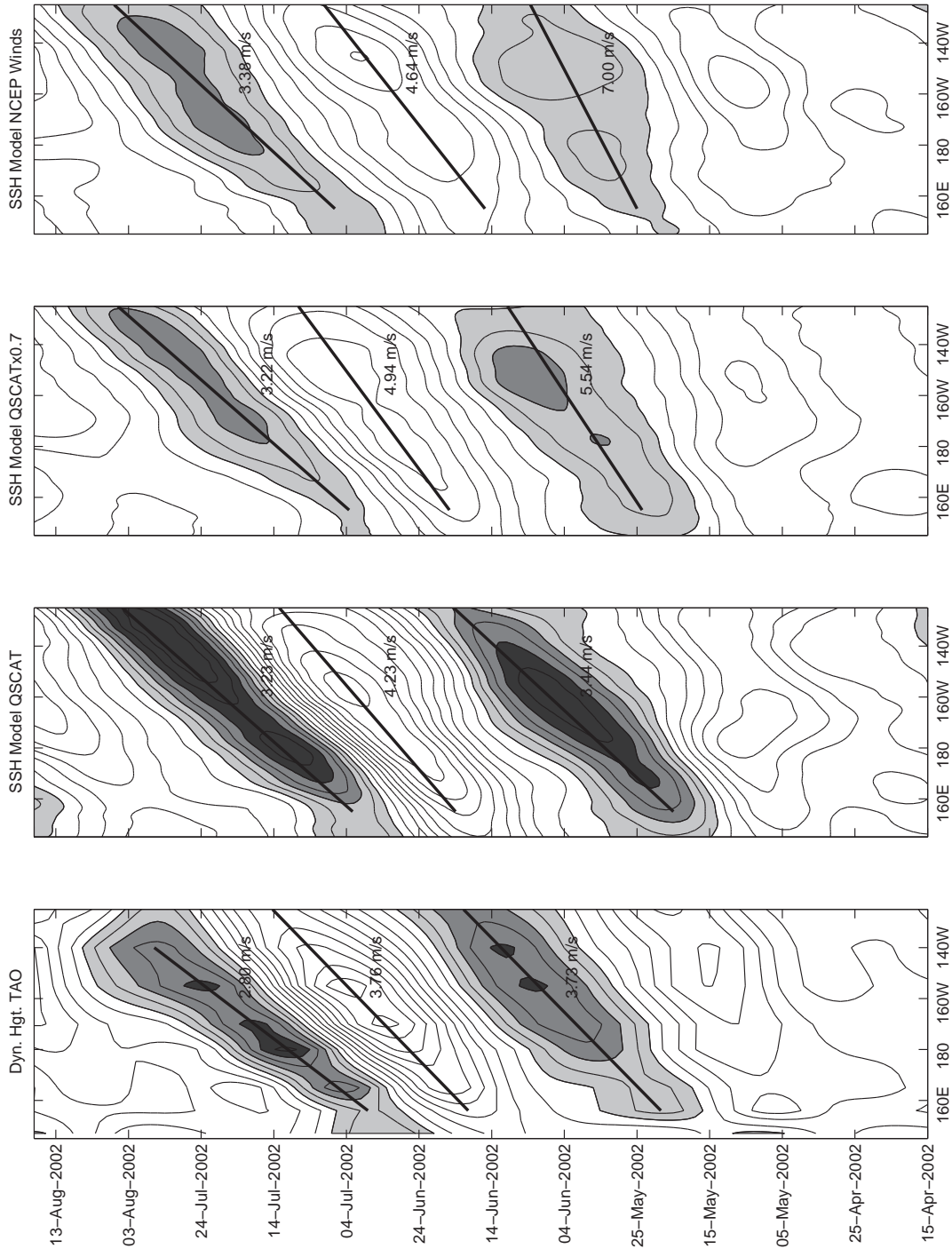


Figure 17: (a) A longitude-time diagram of 20-100 day filtered dynamic height anomalies averaged over 2°N - 2°S from the TAO data during 15 April-31 August, 2002. Lines are trajectories of filtered anomalies and numbers near the lines are corresponding phase speeds. The contour interval is 1.0 cm with minimum contours at ± 0.5 cm. Areas where $\text{SSH} > 1.5$ cm are shaded. (b) Same as (a) except for SSH anomalies from the model experiment forced with QSCAT wind anomalies. (c) Same as (a) except for SSH anomalies from the model experiment forced with QSCAT wind anomalies multiplied by 0.7. (c) Same as (a) except for SSH anomalies from the control experiment.